NASA-CR-193138

NAG8-205

Final Report on
(August 1, 1991 - October 31, 1992)

NUCLEATION AND GROWTH OF ROLLING CONTACT FAILURE OF 440C BEARING STEEL

by

V. Gupta, P.C. Bastias, G.T. Hahn and C.A. Rubin

GRANT
IN-26-CR
167879
p- 64

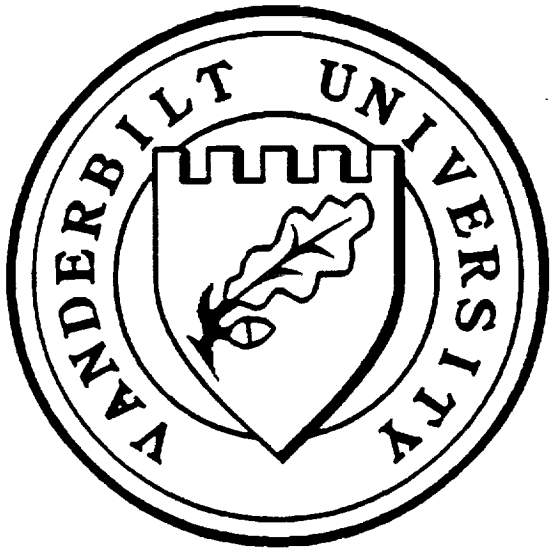

N93-28410
Unclas
G3/26 0167879

CENTER FOR MATERIALS TRIBOLOGY
Vanderbilt University
Nashville, TN

Prepared for:

NASA - MARSHALL SPACE FLIGHT CENTER
Huntsville, AL

December 27, 1992

(NASA-CR-193138) NUCLEATION AND GROWTH OF ROLLING CONTACT FAILURE OF 440C BEARING STEEL Final Report, 1 Aug. 1991 - 31 Oct. 1992 (Vanderbilt Univ.) 64 p

Nucleation and Growth of Rolling Contact Failure of 440C Bearing Steel

by

V. Gupta, P.C. Bastias and G.T. Hahn

ABSTRACT

A "two-body" elasto-plastic finite element model of 2-dimensional rolling and rolling-plus-sliding has been developed to treat the effect of surface irregularities. The model consists of a smooth cylinder in contact with a semi-infinite half-space that is either smooth or fitted with one of 0.4 μm deep or 7 μm deep groove, or a 0.4 μm high ridge-like asperity. The model incorporates elastic-linear-kinematic-hardening-plastic (ELKP) and non-linear-kinematic-hardening-plastic (NLKP) material constitutive relations appropriate for hardened bearing steel and the 440C grade.

The calculated contact pressure distribution is Hertzian for smooth body contact, and it displays intense, stationary, pressure spikes superposed on the Hertzian pressure for contact with the grooved and ridged surface. The results obtained for the 0.4 μm deep groove compare well with those reported by Elsharkawy and Hamrock (1991) for an EHD lubricated contact. The effect of translating the counterface on the half space as opposed to indenting the half space with the counterface with no translation, is studied. The stress and strain values near the surface are found to be similar for the two cases, whereas they are significantly different in the subsurface. It is seen that when tiny shoulders are introduced at the edge of the groove in the finite element model, the incremental plasticity and residual stresses are significantly higher in the vicinity of the right shoulder (rolling direction is from left to right) than at the left shoulder. This may explain the experimental observation that the spall nucleation occurs at the exit end of the artificially planted indents. Pure rolling calculations are compared with rolling + sliding calculations. For a coefficient of friction, $\mu = 0.1$, the effect of friction is found to be small. Efforts have been made to identify the material constitutive relations which best describe the deformation characteristics of the bearing steels in the initial few cycles. Elastic-linear-kinematic-hardening-plastic (ELKP) material constitutive relations produce less net plastic deformation in the initial stages for a given stress, than seen in experiments. A new set of constitutive relations: non-linear-kinematic-hardening-plastic (NLKP) has been used. This material model produces more plasticity than the ELKP model and shows promise for treating the net distortions in the early stages.

Techniques for performing experimental measurements that can be compared with the finite element calculations have been devised. The measurements are being performed on 9mm-diameter, 440C steel cylindrical rolling elements in contact with 12.5 mm-diameter, 52100 steel balls in a 3-ball-rod fatigue test machine operating at 3600 RPM. Artificial, 7 μm deep, indents were inserted on the running track of the cylindrical rolling elements and

profilometer measurements of these indents made, before and after the rolling. These preliminary measurements show that the indents are substantially deformed plastically in the process of rolling. The deformations of the groove calculated with the finite element model are comparable to those measured experimentally.

1. INTRODUCTION

Spalling failure limits the life and performance of the HPOTP bearings in the space shuttle main engine. Lorosch (1982) recognized two distinct modes of rolling contact failure. One is the "far" or the "subsurface" mode which is associated with the contact shear stresses and cyclic plasticity well below the surface. These are described by the Hertzian stresses derived for the contact of idealized, smooth surfaces. The cyclic plastic strains produced by smooth contact are usually vanishingly small at the surface. Failure originates at a depth, $y \approx w$ (2w is the contact width, usually $\approx 500\ \mu m$), below the running surface, where the cyclic strains and fatigue damage peak (Bhargava, 1990). The second is the "near" surface mode which is caused by surface irregularities such as dents and asperities. These defects are attended by pressure spikes (Elsharkawy, 1990, deMul, 1987) superimposed on the Hertzian pressure distribution. These spikes produce cyclic plasticity and more intense fatigue damage within microns of the surface. The near-surface cracks can both nucleate and become surface breaking earlier and are subject to larger crack driving forces, than the far-surface cracks (Shao, 1987). For these reasons, the near surface mode of contact fatigue, which is prevalent in HPOTP bearings (Bhat, 1982), can proceed more quickly than the far surface mode. An example of a near-surface-initiated spall is shown in Figure 1 (Bastias et al. 1992).

These findings emphasize the need for a better understanding of the contribution of surface irregularities to the process of spall nucleation and growth. "One-body" finite element models have been used in the past to study the cyclic plasticity attending rolling-sliding contact loadings (Kumar, 1987 and Bastias, 1990). These models represent the

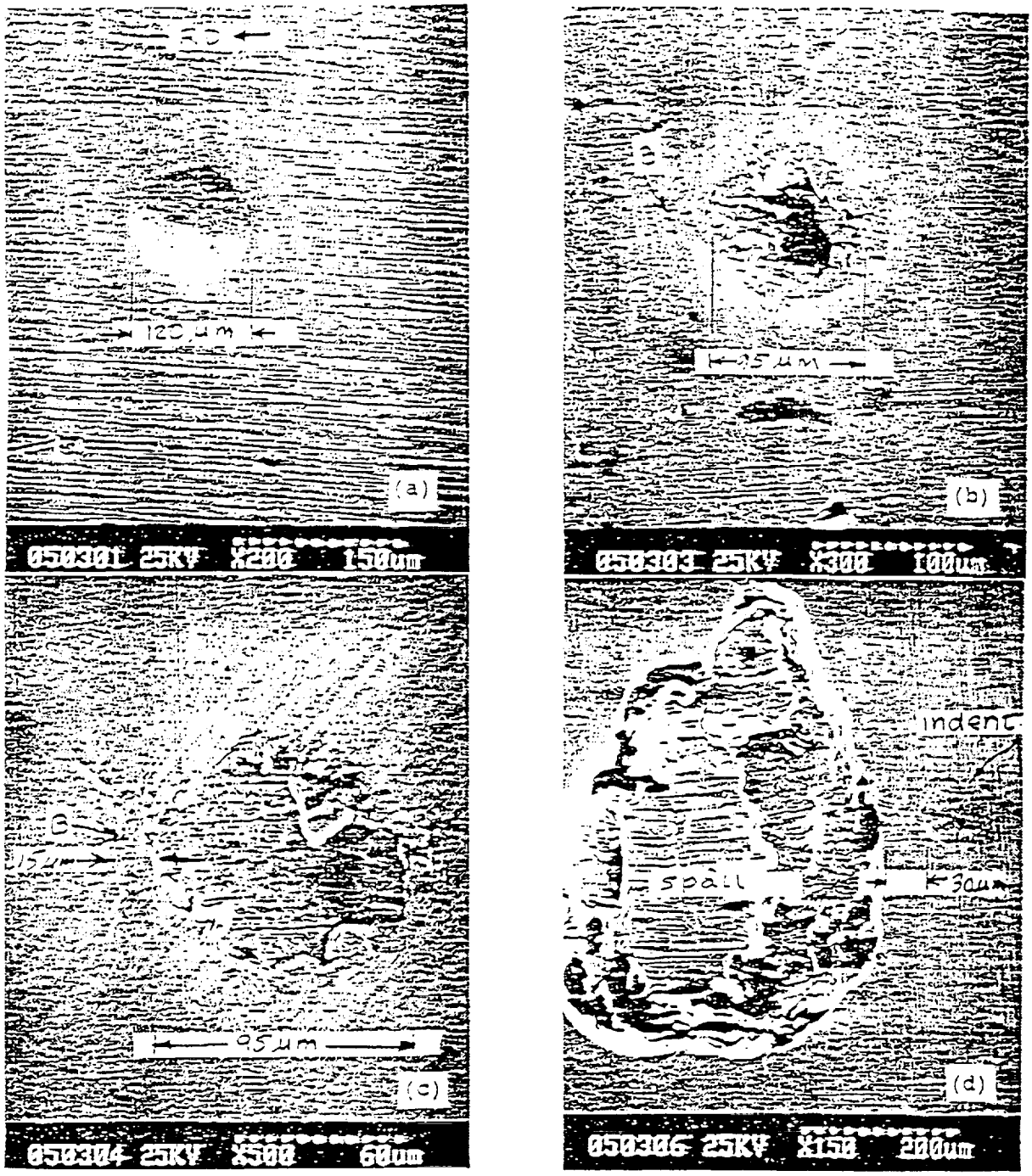

Figure 1 Example of a rolling contact failure nucleated by a 7 μm deep indent in a hardened, 440C steel raceway at a Hertzian pressure of p_0 = 5.4 GPa. (a) Indent before test; original diameter of indent is 120 μm. (b) indent after N = 0.62 x 10^6 contacts; indent diameter has been reduced from 120 μm to 95 μm by plastic deformation (Bastias et al., 1992).

counterface with the corresponding Hertzian pressure distribution which is altered little by plastic deformation. This approach is well suited for treating smooth body, elasto-plastic contacts. It can be extended to treating surface irregularities only when the shape of the pressure distribution produced by the irregularities is known. However,this method cannot account for either the plasticity induced changes in the shape of the asperity or the resulting alterations of the pressure spikes. With this shortcoming in mind , a "two-body" elasto-plastic model of contact has been developed (Leng, 1991), which can incorporate surface irregularities and provide a basis for analyzing the near-surface mode of failure. Results from such a model used to treat the elasto-plastic, dry, rolling contact over a 0.4 μm groove are compared with the calculations published by Elsharkawy and Hamrock (1990), which treated the elastic lubricated contact for the same groove, contact geometry and loading conditions. Fairly good agreement is obtained,thus indicating that the effect of plastic deformation may overweighs the presence of a thin lubrication film.

Laboratory tests, such as the 3-ball/rod test, are used extensively to evaluate the performance of steel for bearing applications. Such tests make it possible to establish the effects of composition, processing, surface modifications and coatings on the final life of rolling elements. However, the current testing methods, coupled with limited analytical capabilities, are a burden. A single test can take weeks (even when the test is accelerated by elevating the contact pressure to as much as 2x the service pressure); months of testing are needed to obtain a single statistically meaningful result. The interpretation of the test result is then complicated by the elevated pressure and other differences between the test and the service conditions: temperature, lubricating conditions, speed, etc. Finally, since

many different material properties simultaneously affect the failure process, even years of testing can fail to provide directions for improving material performance. More understanding of the underlying failure processes and ways of accelerating the testing process are required.

Testing can be accelerated by inserting well characterized defects in the test samples. This would significantly reduce the testing time (by as much as 3x) if only the spall nucleation life in the presence of the artificial defects could be correlated to the nucleation life in the absence of the defects. With this goal in mind, the finite element model described above is used here to study a 7 μm-deep groove in the same geometry and loading conditions as those present in the 3 ball/rod testing machine. A similar 7 μm-deep groove is inserted in the rolling elements used for the experiments. The aim is to compare the finite element results directly with those from the RCF tests.

2. ANALYTICAL AND EXPERIMENTAL PROCEDURES

2.1 Finite Element Models

2.1.1 Model 1 (Shallow Groove):

The present model is a modified form of the one used by Leng (3). As described in the previous report (8), the original mesh was reduced in size and refined in the proximity of the indent. In order to model an asperity as shallow as the one studied by Elsharkawy and Hamrock (5), approximately 0.4 μm, it was necessary to further refine the mesh. Both, the half space and the cylinder have been refined (see Figure 2). The dimensions of the

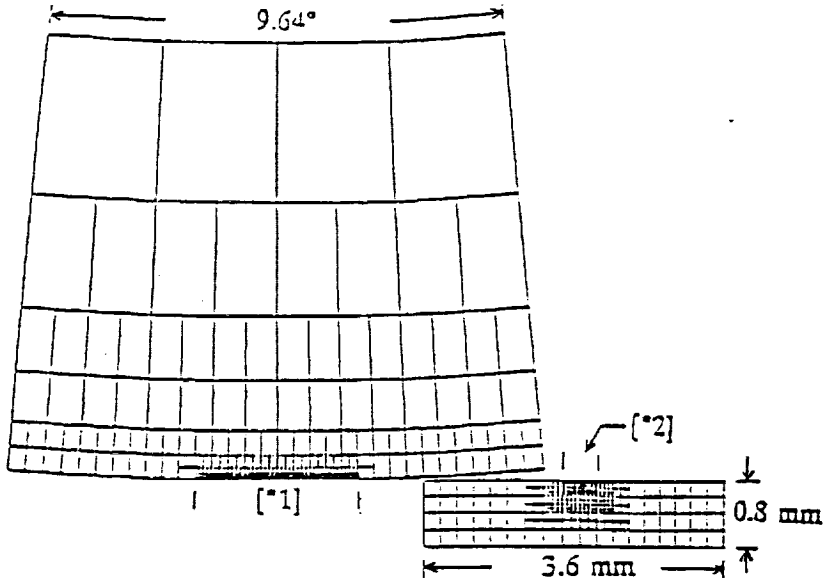

Figure 2 The finite element mesh (model 1) used to study the shallow groove. The regions designated as [*1] and [*2] are shown magnified in Figures 3(a) and 3(b), respectively.

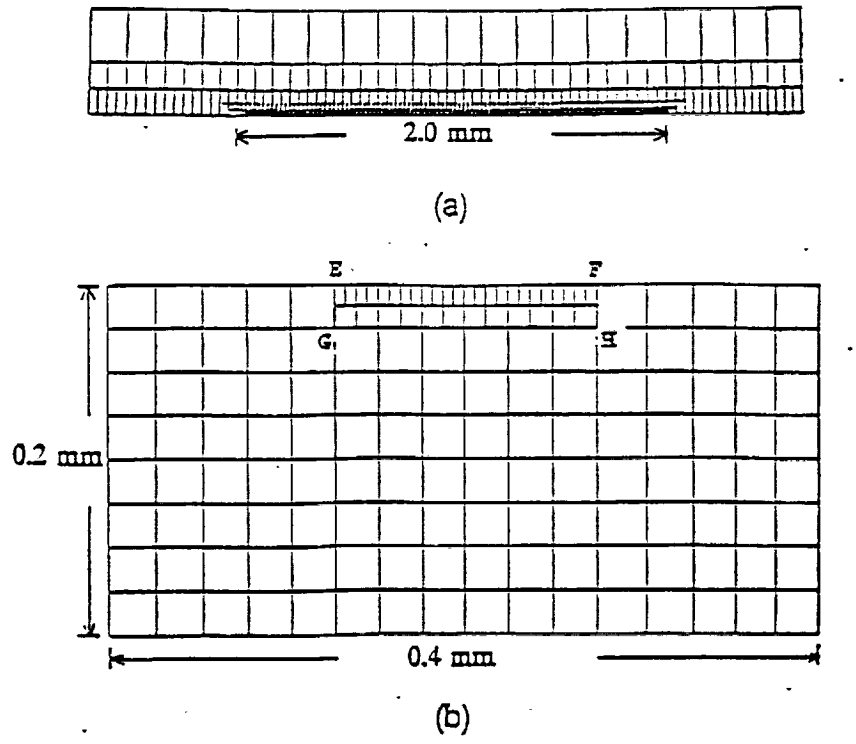

Figure 3 Magnified view of the regions designated as (a) [*1] and (b) [*2] in Figure 2.

elements near to the indent have been reduced to $1/4^{th}$ of those in the previous mesh. This brings the length of the smallest element to 6.25 micron on both the half-space and the counterface. To keep the number of elements as small as possible the cylinder has been refined only in the region where it contacts the half space.

The current mesh is made up of 1375, eight noded plane strain elements, 246, quadratic interface elements and a "slide-line" covering the contacting surface of the half space. The mesh has 3801 nodes.

Boundary conditions applied to the mesh to simulate the rolling of the cylinder over the half space have been simplified. Previously, the boundary displacements for both bodies (the indented half space and the cylinder) were obtained from the calculations for the smooth surfaces under similar loading conditions. This necessitates a smooth surface calculation before any calculation for the indented surface can be carried out. It has been observed in previous calculations that the plastic deformation near to the boundaries is negligible and therefore for the recent calculations, the boundaries of the half space are displaced elastically. The load distribution is broken into several hundred concentrated forces. The elastic displacements due to each of these forces is calculated at the boundary nodes (using closed form solutions) and superposed. This procedure is programmed in the user subroutine 'DISP', and included in the 'ABAQUS' input file.

Finite element calculations have been performed for dry, two body contact using the more refined mesh described above. The calculations examined the same indent, contact geometry and loading conditions whose (elastic) lubricated contact was treated by Elsharkawy and Hamrock (1990). The indent geometry and loading conditions for the

calculation are summarized in Table 1.

Both elastic and elasto-plastic FEM calculations have been performed. The elastic calculations basically involve indentation of the half-space, containing the asperity, with the cylinder. The asperity is indented with the center of the cylinder located 0.5w[1] away (in the rolling direction) from the center of the asperity. This is the off-center position at which Elsharkawy and Hamrock have reported their results. This procedure is appropriate for the elastic calculations only.

Since the plastic deformation is dependent on the loading history, the translation of the cylinder over the half-space is important for the elasto-plastic calculations. The authors

Table 1. Indent geometry, loading conditions and material properties used in the calculations using model 1.

Radius of the Cylinder (R)	38.0 mm
Total Pressure (P)	5.64×10^{05} N/m
Peak Pressure (p_0)	733.0 MPa
Half Contact Width (w)	490.0 μm
Semi Width of the Asperity (x_w)	50.0 μm
Maximum Depth of the Asperity (Z_m)	0.4 μm
Elastic Modulus (E)	207.0 GPa
Poisson's Ratio (ν)	0.3
Kinematic Yield Strength (σ_k)	275.0 MPa
Plastic Modulus (M)	378.0 MPa

[1] Where 'w' is the half contact width.

wish to study the effect of this history dependence on the peak plasticity produced. To this end, the calculations with and without translation have been compared.

The following plastic calculations have been performed:

(i) Plastic Calculation 1 (PC1)- The half-space is indented with the center of the cylinder coinciding with the center of the asperity.

(ii) Plastic Calculation 2 (PC2)- The half-space is indented with the center of the cylinder coinciding with the center of the asperity. With the load still applied, the cylinder is then translated in the rolling direction by 0.5w to reach the off center position.

(iii) Plastic Calculation 3 (PC3)- The half space is indented directly at the off-center position. i.e., the cylinder is moved by 0.5w in the rolling direction and then the indentation is made.

(iv) Plastic Calculation 4 (PC4)- This calculation is performed for the same conditions as PC1, PC2 and PC3 but without the presence of the asperity. The objective of the calculation is to determine the effect of the asperity on the sub-surface stresses and strains produced.

2.1.2 Model 2 (Deep Groove):

This model is the modified form of model 1 described above (Figures 2 and 3). The mesh has been further refined near the groove to increase the accuracy of the results (see Figure 4). The radius of the cylindrical body (counterface) indenting the (flat) half space has been suitably modified so that the finite element calculations can be compared to the rolling contact fatigue (RCF) tests. The new cylinder radius of 2.4 mm produces a contact patch

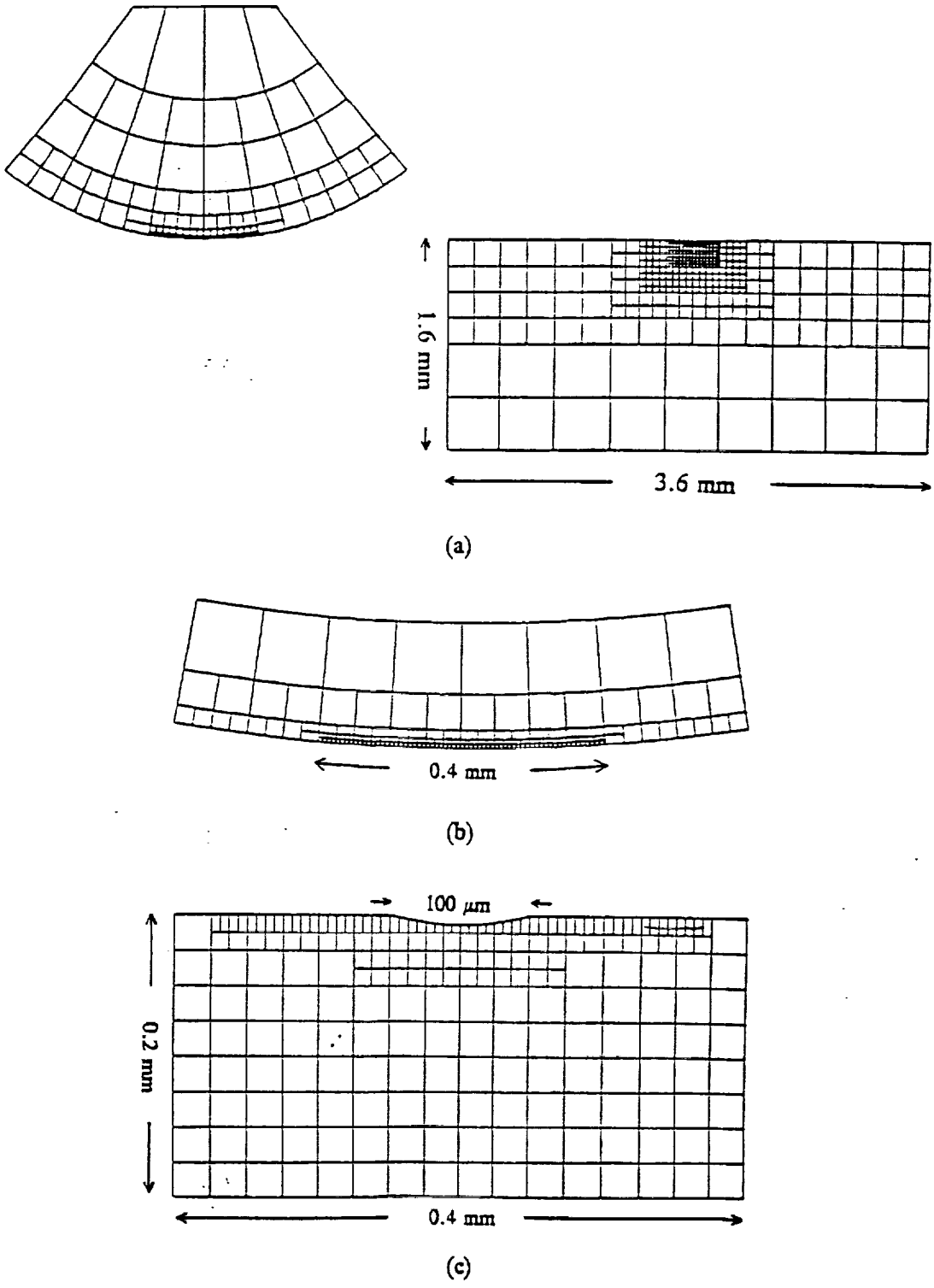

Figure 4 The finite element mesh used to study the deep groove. (a) the counterface with a radius of 2.4 mm and the half space, (b) magnified view of the refined region of the counterface and (c) magnified view of the refined region of the half-space containing the indent.

in plane strain (2-D) finite element calculations, the width of which in the rolling direction corresponds to the width of the contact patch produced by 12.5 mm diameter balls in contact with a 9 mm diameter rod shaped sample in the RCF test machine (3-D). Details of the contact geometry may be found in Appendix A.

Most of the procedures and boundary conditions used for the finite element calculations are similar to those in model 1. A new procedure has been used to determine the total applied load corresponding to a predetermined radial displacement of the contacting cylinder. The finite element formulation specifies a vertical displacement to the counterface and applies suitable boundary conditions to the half space to accomplish the loading step. The load corresponding to a applied displacement is ascertained by measuring the contact width and the peak pressure produced due to the displacement and then comparing them with the theoretically calculated values (elastic). This procedure is very accurate when the material properties of the model are stiff enough and do not deviate significantly from the elastic solution. But in current calculations very compliant material properties were used to simulate the high amount of plasticity seen in the initial few cycles. This causes the pressure distribution to deviate from the Hertzian (elastic) distribution. In such a case the contact width is significantly wider and the peak pressure lower than the elastic calculated values. For a plot of normalized pressure distribution (p/p_o) versus the normalized coordinate (x/w) the area under the curve can be shown to be $\pi/2$ for perfectly Hertzian distribution (elastic). This area is a measure of the total load. For an inelastic distribution, the correct total load is achieved when the area under the normalized pressure distribution equals $\pi/2$.

A computer program using a cubic spline algorithm was written. The program fits a polynomial through the pressure distribution and then integrates the polynomial to calculate the area under the curve. The cubic spline algorithm is especially suited for our case because of the presence of the pressure spikes in the distribution. Fitting a single polynomial through the whole distribution would yield very inaccurate results. The cubic spline algorithm fits a different cubic polynomial between each pair of two successive data points.

Two-body finite element calculations, on a grooved half-space, for rolling and rolling-sliding contact have been performed. Both ELKP and NLKP material models were investigated. The abbreviations used in the calculation titles are as follows:

P -	ELKP material model.
NL -	NLKP material model.
1 or 2-	Number of successive contacts.
I -	Indentation (no translation).
T -	Translation.
A -	Contact with asperity.
N -	No asperity; Smooth contacting surfaces.
F -	Rolling with frictional sliding.
S -	Built up shoulders around groove.

The following calculations have been performed:

(a) P1IA and P2IA The half space is indented with the center of the counterface coinciding with the center of the asperity. The loading is applied by displacing the counterface vertically onto the half space until the required load is achieved (verified by measuring the area under the curve). The half space is then unloaded by displacing the counterface vertically up to the original position. This loading and unloading constitutes calculation P1IA. The half space is reloaded and then unloaded to perform calculation

P2IA.

(b) P1TA and P2TA The half space is indented with the center of the counterface 2w to the left of the center of the asperity. The required pressure is achieved as described above. The counterface is then translated horizontally to the right so that it rolls over the asperity. Translation is stopped when the center of the counterface reaches 2w to the right of the center of the asperity. The half space is then unloaded by displacing the counterface upwards to its original position. This completes calculation P1TA. The whole procedure is again repeated to accomplish the second cycle - P2TA.

(c) P1TN and P2TN These calculations are performed without the presence of the asperity. These calculations simulate rolling in the absence of defects. The procedure for these calculations is exactly the same as for P1TA and P2TA. The motivation for these calculation was to make a comparison of the results with and without the presence of the asperity and thus isolate the effect of the asperity.

(d) P1TAF and P2TAF Frictional traction has been introduced in these two calculations. The procedure for these two calculations is again the same as P1TA and P2TA except that a coefficient of friction, $\mu = 0.1$ is introduced.

(e) NL1IA and NL2IA This calculation has been performed with non-linear-kinematic-hardening-plastic (NLKP) material property constitutive relations. The NLKP model produces significantly more plasticity (3-4 times higher) than the ELKP model. The NLKP results come closer to the experimentally observed values than the ELKP results and may be better suited to model the initial transient period (the first few revolutions during which the bulk of incremental plasticity occurs).

(f) P1IAS and P2IAS In these calculations, shoulders at the edges of the indent are introduced in the finite element mesh. The profile of the shoulders is measured from profilometer measurements. ELKP constitutive relations were used but with a low plastic modulus, M (75 GPa), calculated from Figure B1 (Appendix B) for the amount of strain expected in the calculation.

(g) NL1IAS Calculation was similar to (f) but with NLKP constitutive relations. Table 2 lists the indent geometry and loading conditions for the calculations using model 2. Calculation sets (a) to (d) are performed for ELKP (set 1) material properties, calculations (e) and (g) for NLKP properties and calculation set (f) for ELKP (set 2) material properties. The ELKP and NLKP parameters are listed in Tables 3 and 4, respectively. A description of the NLKP parameters can be found in Appendix B.

2.2 Experimental Procedures

2.2.1 Material Used:

The rolling experiments were carried out on the 3-ball-rod rolling contact fatigue tester developed by the ball and roller bearing group at Federal-Mogul, and furnished by NTN Bower. The design and operation of the tester machine has been described by Glover (1982).

The test material is AISI 440C, martensitic stainless steel, heat treated to a hardness of 55-57 HRc. The test samples were subjected to the following heat treatment:

(a) Austenized at 1930$\pm$30 °F for 1 hour.

(b) Quenched in liquid nitrogen.

Table 2 Indent geometry and loading conditions for the finite element calculations using model 2.

Radius of the Cylinder (R)	2.4 mm
Total Load (P)	1.55 MN/m
Peak Pressure (p_0)	4.85 GPa
Half Contact Width (w)	204.0 μm
Semi Width of the Asperity (x_w)	50.0 μm
Maximum Depth of the Asperity (Z_m)	7.0 μm

Table 3 ELKP Parameters

PARAMETER	SET 1	SET 2
E (Elastic Modulus)	207.0 GPa	207.0 GPa
σ_k (Kinematic Yield Strength)	1050.0 MPa	1050.0 GPa
M (Plastic Modulus)	188.0 GPa	75.0 GPa

Table 4 NLKP Parameters.

PARAMETER	VALUE
E (Elastic Modulus)	207.0
ν(Poissons Ratio)	0.3
μ(Rate Constant Isotropic Hardening)	7.37
R (Cyclically Stable Yield Surface Radius)	970.0 MPa
b (Cyclically Stable Amplitude of Short Range Backstress)	050.0 MPa
H^* (Coefficient of Linear Hardening for Long Range Backstress)	50.0 MPa
kl (Coefficient of short range backstress rate)	970.0

Note: For this model b(0) = b, R(0) = R, assuming cyclically stable conditions.

(c) Tempered for one hour (minimum) at 325±25 °F.

(d) Air cooled to 70±10°F.

(e) Cold soaked in liquid nitrogen for 30 minutes.

(f) Tempered for 1 hour at 325±25°F.

The geometry of the sample is shown in Figure 5. Each sample can be used to perform upto 8 individual tests. The samples have a surface finish of 0.12 μm, roundness of 2.54 - 3.80 μm and a peak-to-valley value of 0.8 μm (see Figure 6). The balls used in the RCF tester are made of AISI 52100 bearing grade steel. The balls have a surface finish of 0.34 AA (8.6×10^{-3} μm). The chemical composition of both the 440C and the 52100 steels are shown in Table 5. Exxon grade 2380 turbine oil was used as a lubricant for all the tests. The oil was applied by drip feed at a rate of 10 drops per minute. The tests were carried out at a peak Hertzian pressure of 4.85 GPa.

The running tracks of the specimens were artificially dented by a 120° sphero-conical Rockwell "Brale" penetrator. The load applied to obtain the hardness indents was

Table 5 Composition of 440C and 52100 steels.

Steel	C	Mn	Si	Cr	Ni	Mo	Cu	Al	P	S
440C	1.05	0.44	0.44	17.11	0.1	0.48	0.04	0.02	<0.022	<0.001
52100	1.02	0.34	0.32	1.45	0.13	0.05	0.16	—	<0.09	<0.014

Balance Fe

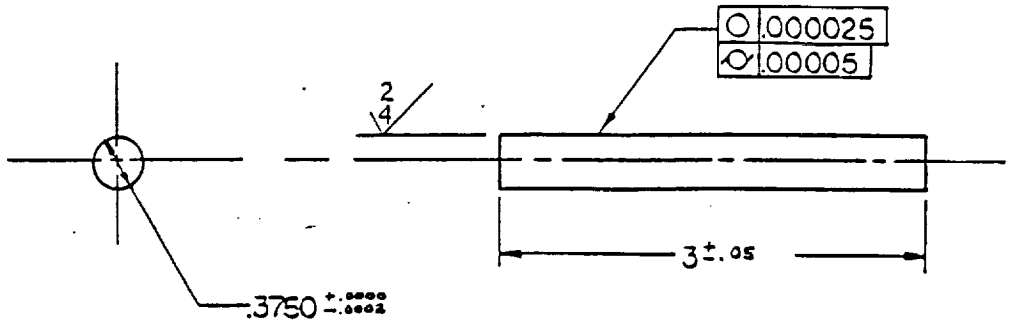

Figure 5 Test specimen design according to Glover (1982), all the dimensions are in inches.

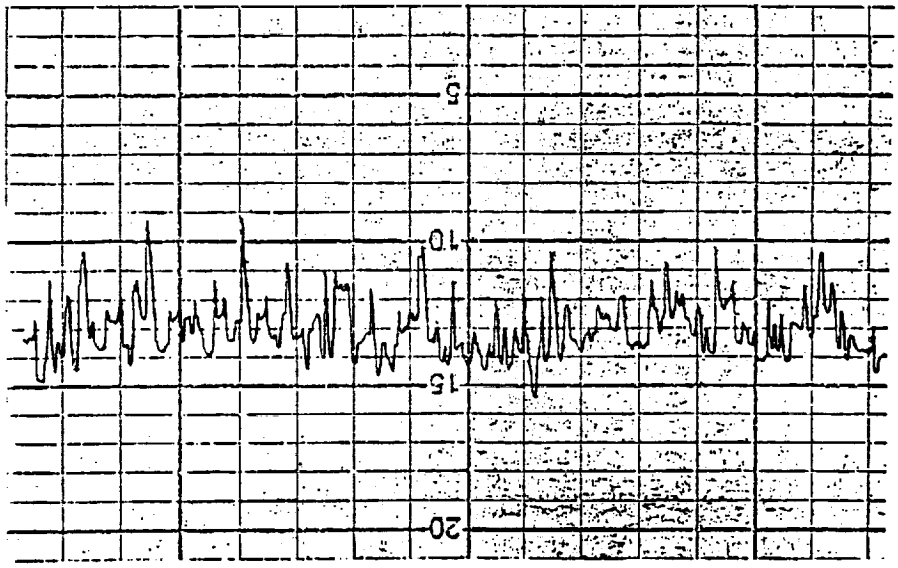

Figure 6 Profilometer trace of a RCF sample showing a peak-to-valley value of 0.8 μm. Vertical magnification = 20000x, horizontal magnification = 100x.

approximately 10 kg, and the diameter of the indentation was approximately 0.1 mm.

2.2.2 Surface Profile Measurements

The surface profiles were measured using a Talysurf 10 profilometer manufactured by Rank Taylor-Hobson Limited. The diamond stylus has a tip width of 0.0025 mm and an overall system accuracy of $\pm 2\%$ of the 'full scale displacement'. The instrument was calibrated using a 'calibrated standard' before the measurements were made. A 'Goniometer' is used to hold the sample so that it can be rotated about its axis by fixed amounts.

Recently, the Talysurf has been successfully interfaced to a computer. The analog signal from the Talysurf containing the 'profile' is fed into the computer. A DT-2821 series board is used for the analog-to-digital conversion of the data. The digitized data is then displayed and further processed on the computer screen using the software 'Global Lab'. Figure 7 illustrates the procedure used for calibrating the digitized data (obtained in millivolts as a function of time). The millivolts correspond to the vertical dimension of the profile (height or depth of the surface feature), and the seconds correspond to the horizontal dimension (distance traversed by the stylus). Since the stylus moves at a constant velocity, the seconds are easily converted to distance by multiplying them by the velocity of traverse. To calibrate the vertical dimension, a standard calibration sample is used. The Talysurf was run over the standard sample consisting of three lines, the height of the central line being exactly 2.33 μm. The signal collected is shown in Figure 7(a). This implies that 135.306 mV = 2.33 μm. Figure 7(b) shows the corresponding trace obtained on the chart.

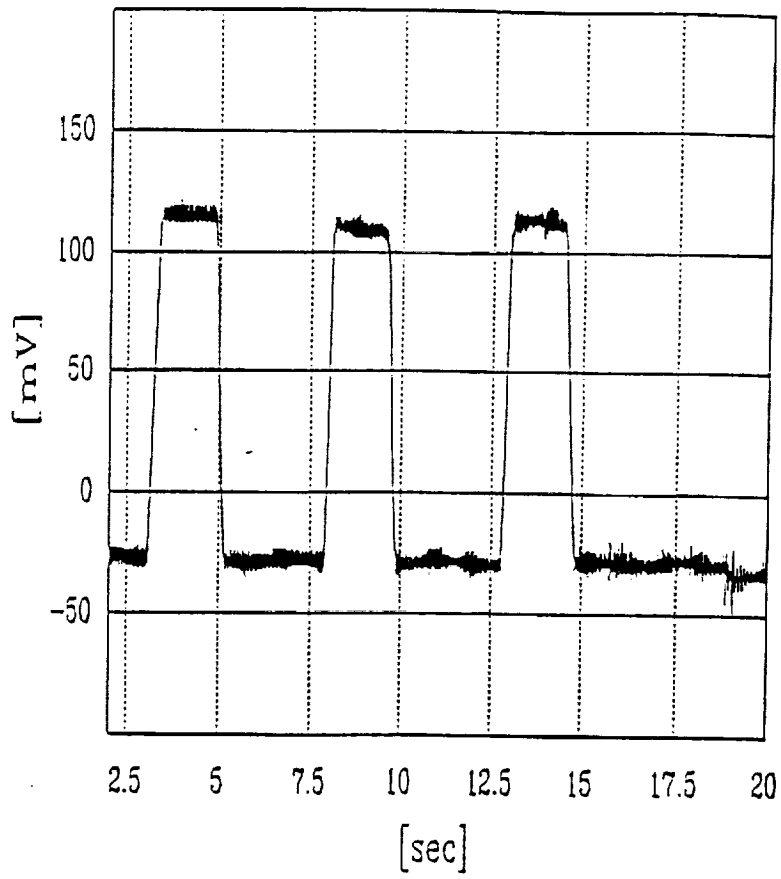

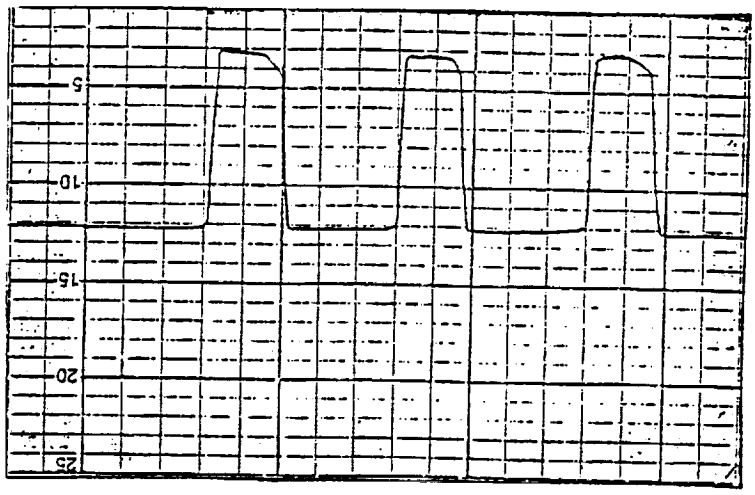

Figure 7 The profile of the calibration standard with the center line height of 2.33 μm (a) Millivolts versus seconds plot from the data acquiesced by the computer and(b) the profilometer trace of the calibration standard at a vertical magnification of 10000x.

3. RESULTS

3.1 Finite Element Calculations

3.1.1 Results for 0.4 μm-Deep, Shallow Groove (Model 1)

Figure 8 compares the pressure distribution derived from the elastic finite element calculations for dry contact, with the distributions reported by Elsharkawy and Hamrock for lubricated EHD contact. The general shape of the distributions are similar but peak pressures differ significantly. The differences in the peak pressures and the load supported at the bottom of the indent may have two sources. The 0.7 μm lubricant film over the indent supports more pressure thereby reducing the spikes and the degree of refinement of the two models may be different. Figure 9 compares the pressure distribution under the contact for the elastic and the elasto-plastic (PC2) FEM calculations. Plastic deformation of the indent is seen to reduce the peak pressure considerably. The contact width is slightly increased as a result of plastic deformation. Figure 10 shows the pressure distributions for the PC2 and PC3 calculations. A slight forward flow is evident for PC2. Further, the height of the pressure spikes is modified. Figure 11 shows the pressure distribution for the elastic finite-element calculation for a bump. Figure 12 shows the Mises stress contours for PC1 and PC4 calculations. Figure 13 shows the equivalent plastic strain contours for PC1 and PC4 calculations, on the whole half space. Figure 14 shows the equivalent plastic strain contours, for PC1, PC2 and PC3 calculations, on a small section of the half-space. The plastic strain peaks directly beneath the edges of the asperity for calculations with the asperity (PC1, PC2 and PC3) and right below the center of the cylinder for the smooth calculation (PC4). The magnitude and location on the half-space, of the peak Mises stress,

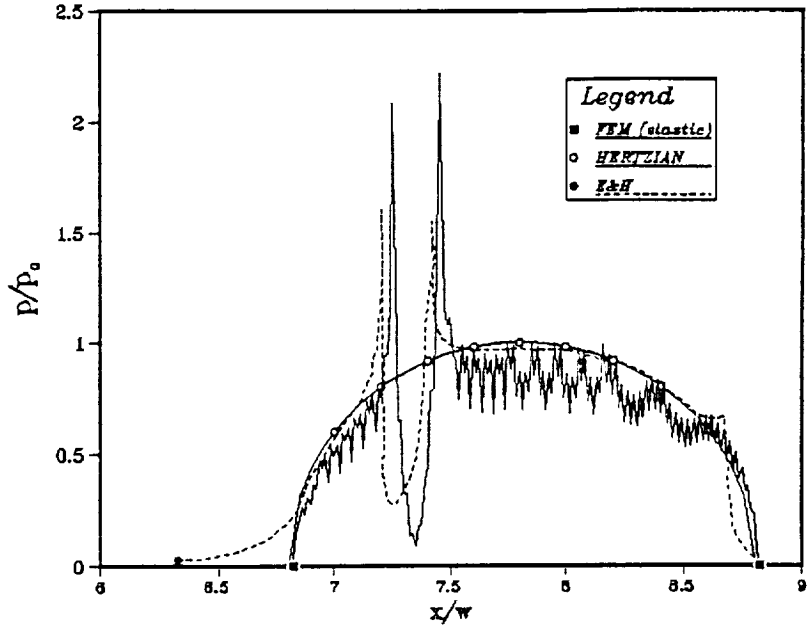

Figure 8 Normalized pressure, p/p_0, versus normalized x-coordinate, x/w. Results from elastic finite element calculations (model 1), Elsharkawy and Hamrock and the pure Hertzian pressure distribution are superposed.

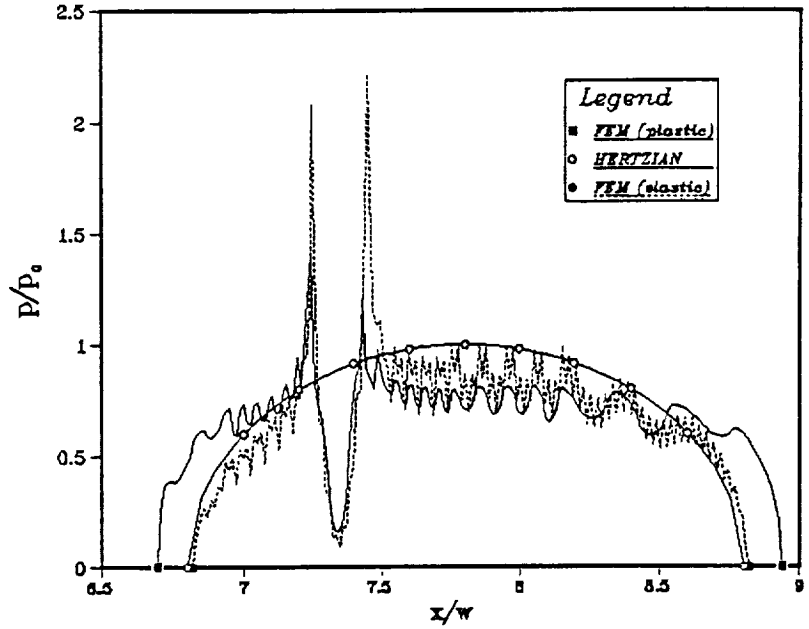

Figure 9 Normalized pressure, p/p_0, versus normalized x-coordinate, x/w. The plastic (PC3) and elastic finite element results (model 1), along with the pure Hertzian distribution, are superposed.

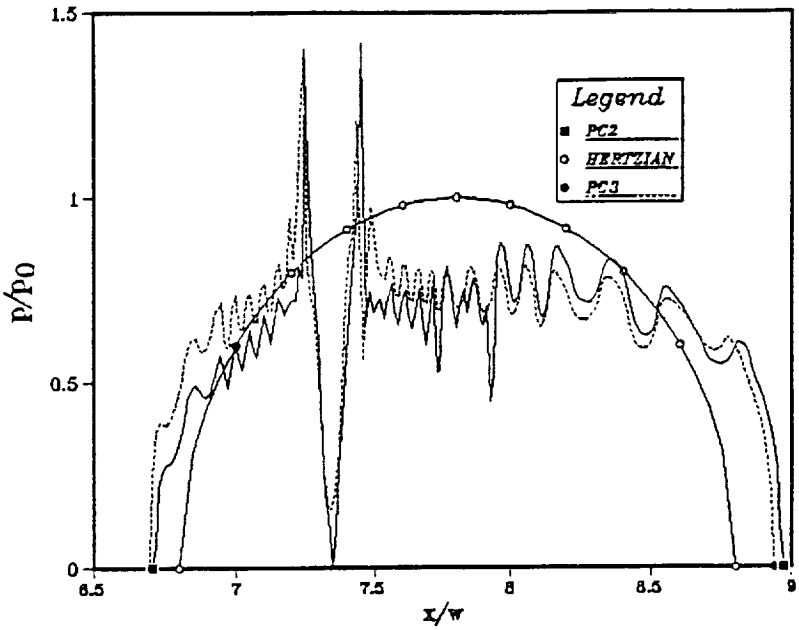

Figure 10 Normalized pressure, p/p_0, versus normalized x-coordinate, x/w. The Plastic, PC2 (indentation and translation) and PC3 (indentation only) finite element results (model 1) and pure Hertzian pressure distribution are superposed.

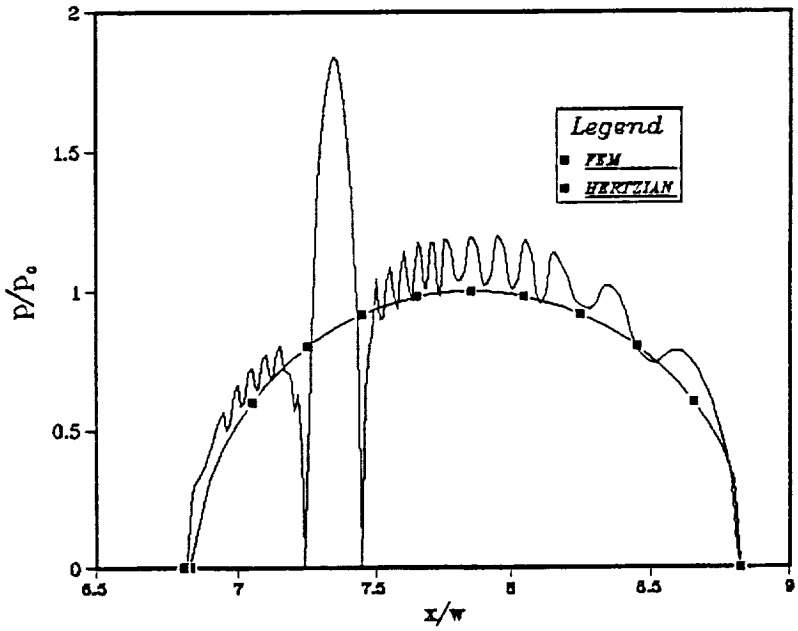

Figure 11 Normalized pressure p/p_0 versus normalized x-coordinate, x/w. Elastic finite element calculations for a bump (model 1) and pure Hertzian pressure distribution are superposed.

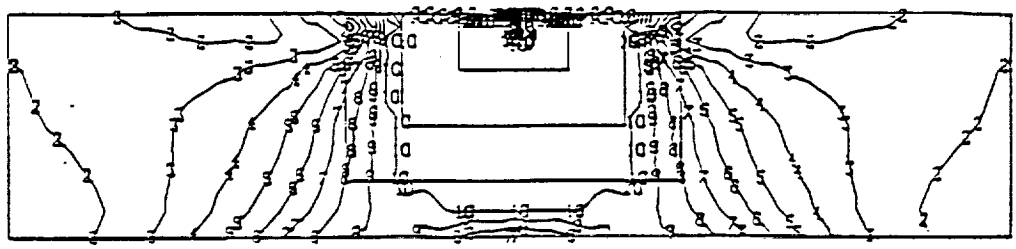

(a)

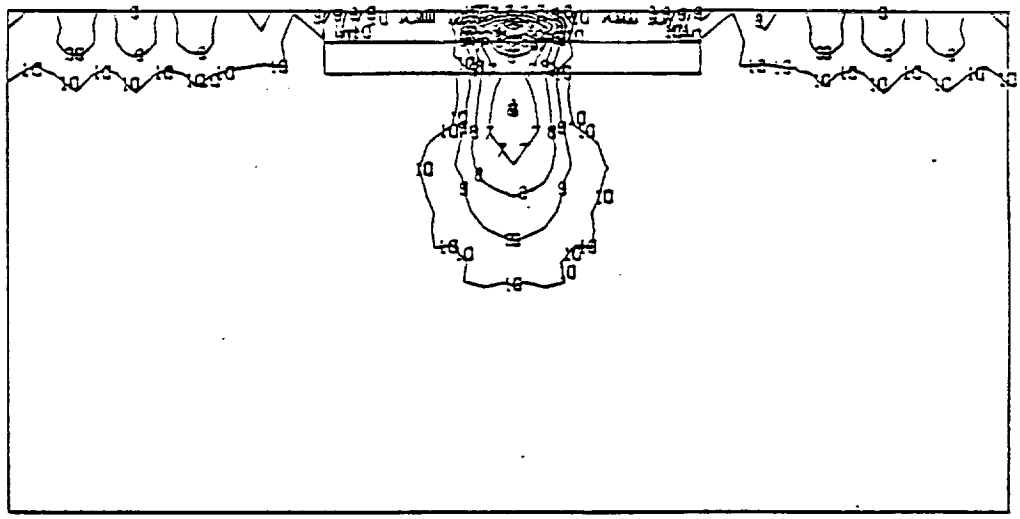

MISES

	VALUE
1	+3.00E+01
2	+3.00E+07
3	+6.00E+07
4	+9.00E+07
5	+1.20E+08
6	+1.50E+08
7	+1.80E+08
8	+2.10E+08
9	+2.40E+08
10	+2.70E+08
11	+3.00E+08

(b)

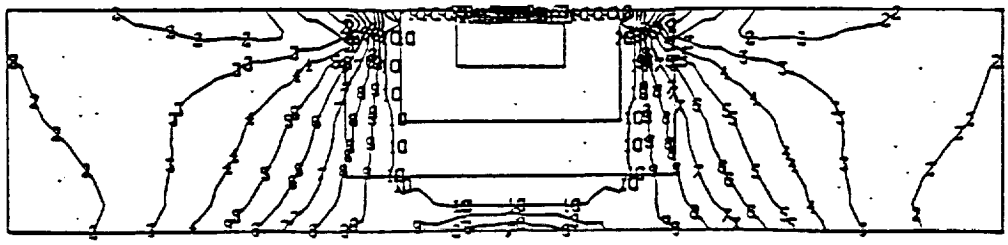

(c)

Figure 12 Mises Stress iso-contours for the half space for the plastic, (a) PC1 (indentation at the center), (b) PC1, for a small portion of the mesh (region in Fig. 2(b)) and (c) PC4 (no asperity) calculations.

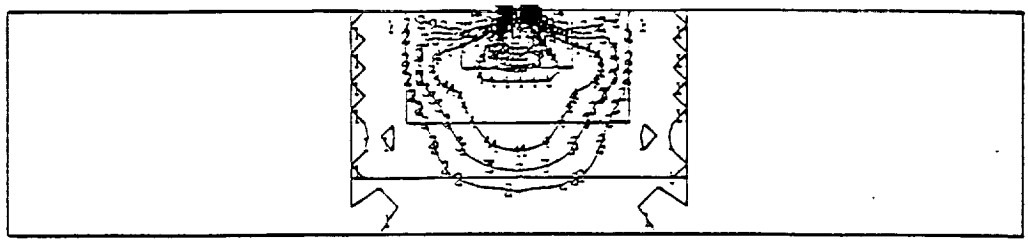

(a)

PEEQ	VALUE
1	+5.00E-10
2	+5.00E-04
3	+1.00E-03
4	+1.50E-03
5	+2.00E-03
6	+2.50E-03
7	+3.00E-03
8	+3.50E-03
9	+4.00E-03
10	+4.50E-03
11	+5.00E-03

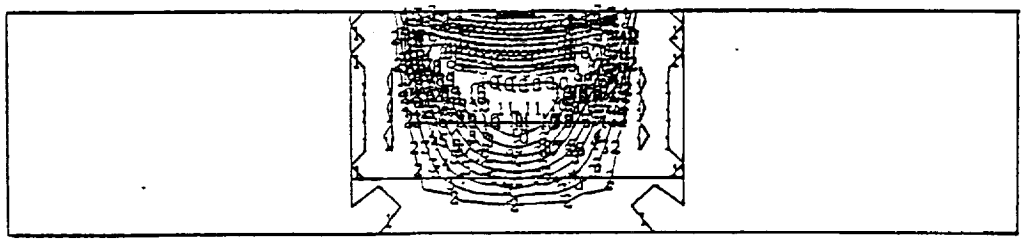

(b)

PEEQ	VALUE
1	+2.00E-10
2	+2.00E-04
3	+4.00E-04
4	+6.00E-04
5	+8.00E-04
6	+1.00E-03
7	+1.20E-03
8	+1.40E-03
9	+1.60E-03
10	+1.80E-03
11	+2.00E-03

Figure 13 Equivalent plastic strain iso-contours for the half space for the plastic, (a) PC1 (indentation at the center) and (b) PC4 (no asperity) calculations.

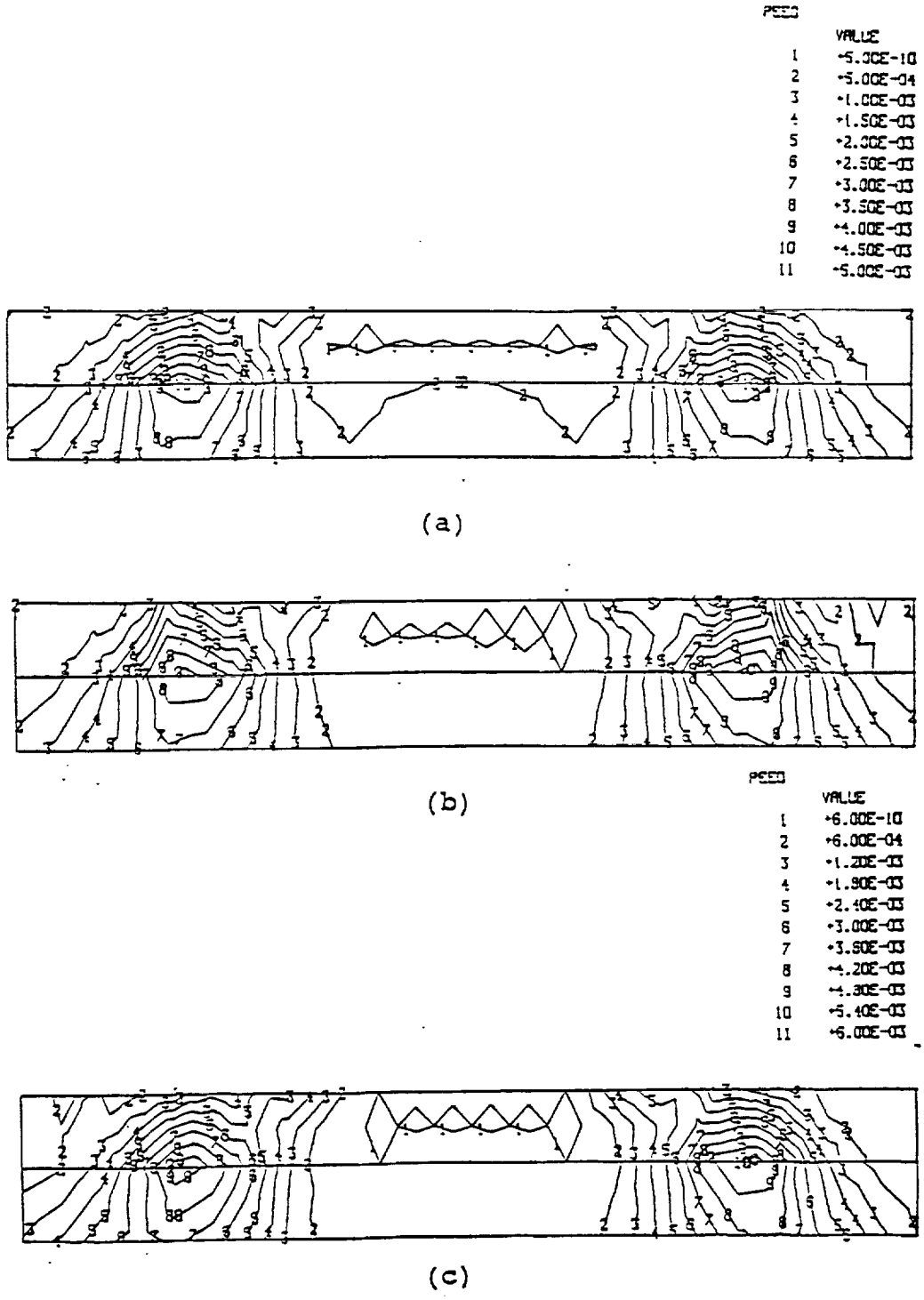

Figure 14 Equivalent plastic strain iso-contours for a small portion of the half space (region EFGH in Fig. 2(b)), for plastic, (a) PC1 (indentation at the center), (b) PC2 (indentation and then translation) and (c) PC3 (indentation directly at the off-center position).spikes is modified.

equivalent plastic strain and shear stress are tabulated in Table 6 for the various calculations.

Figure 13 and Table 6 illustrate that the peak plastic strain below the groove: 4.2 x 10^{-03} (PC1), is 2x as large as for the smooth surface: 2.0 x 10^{-03} (PC4). The depth at which the peak plasticity occurs is also very different. It changes from sub-surface in PC4 (375 μm) to near surface in PC1 (13.2 μm). In other words, the asperity not only increases the peak plastic strain by more than 2x, it also generates the peak strain very close to the surface. The continuing cyclic plasticity occurs close to the surface at a depth, $Y_0 \sim A.h$, where $2 < A < 60$, and h corresponds with the height or depth of the irregularity. Table 7 lists a summary of A-values based on the work of various researchers: Leng (1990), de Mul (1987), Elsharkawy (1990) and Lubrecht (1990). Clearly, a simple, consistent picture has not yet emerged.

3.1.2 Results for Model 2 (Deep Groove)

(a) Comparison of the Effect of Translation and Indentation in the Presence of a groove (ELKP Material)

Figures 15 and 16 compare the distribution of circumferential and in-plane shear residual stresses, σ_{ij}/k, with normalized depth, y/w, after 2 successive contacts. Three cases are illustrated: (i) Repeated frictionless indentation of the groove by the counterface (P2IA), (ii) Repeated frictionless rolling contact over the grooved surface (P2TA) and (iii) Repeated frictionless rolling contact over a perfectly smooth surface (P2TN). The results show that for the case of translation (P2TA), the effects of the groove on the circumferential residual

Table 6 Location of the Maximum Mises stress, equivalent plastic strain and shear stress in the half-space. Location of the center of the indentor (cylinder) is 3.6 mm for PC1 and PC4 and 3.835 for PC2 and PC3. The edges of the asperity are at 3.55 and 3.65 mm.

		PC1	PC2	PC3	PC4
Value of Maximum Mises Stress (MPa)		288.0	290.2	291.8	281.0
Location of Max. Mises Stress.	x y	3.55 mm -16.0 μm	3.64 mm -15.9 μm	3.55 mm -12.7 μm	3.60mm -395 μm
Value of Max. Plastic Strain. ($x10^{-03}$)		4.22	5.42	5.32	2.0
Location of Max. Plastic Strain.	x y	3.55 mm -13.2 μm	3.65 mm -13.1 μm	3.65 mm -12.9 μm	3.60mm -376 μm
Value of the Max. Shear Stress (MPa).		134.0	139.0	131.0	132.0
Location of the Max. Shear Stress.	x y	4.05 mm -189 μm	4.3 mm -223 μm	4.3 mm -378 μm	4.05 mm -189 μm

Table 7. The Calculated depth of the strain concentrations produced by elastic rolling contact with surface irregularities.

Irregularity Type	Irregularity Height or Depth, h, μm	Depth of Peak Plastic Strain Activity, Y_o,μm	$A=y_o/h$	Reference
Indent	40	80	2	de Mul, et al. (4)
Indent	3	~10	~3	Lubrecht, et al. (9)
Indent	7	~25	3.5	Leng, et al. (3)
Indent	0.4	<14	<35	Elsharkawy and Hamrock (5)
Indent	0.4	13.1	~33	Present study
Bump	0.4	~24	~60	Elsharkawy and Hamrock (5)

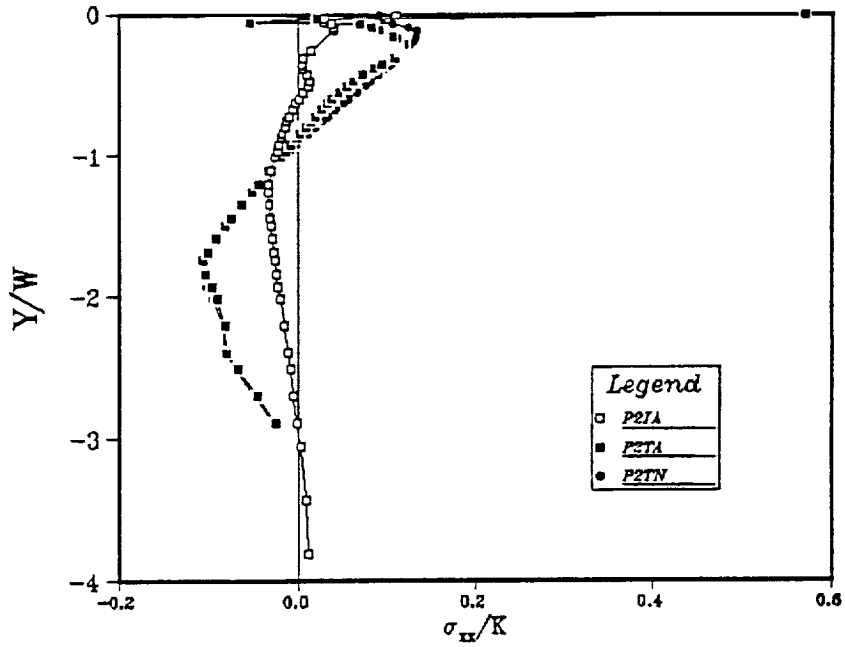

Figure 15 Variation of normalized residual circumferential stress, σ_{xx}/k, with normalized depth, y/w, after 2 contacts (model 2 - deep groove).

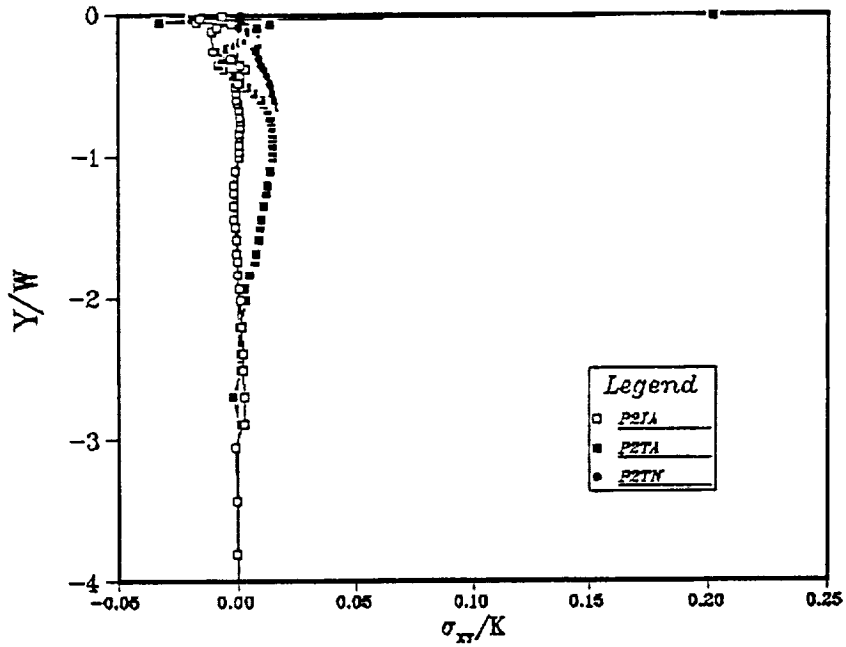

Figure 16 Variation of normalized residual shear stress, σ_{xy}/k, with normalized depth, y/w, after 2 contacts (model 2).

stresses are confined to shallow depth, $y/w < 0.2$. For the in plane residual shear stresses the effect vanishes for $y/w > 0.6$. Figure 17 shows the accumulated equivalent plastic strain variation with normalized depth, after 2 cycles. Notice the near and the subsurface concentration of strain. Calculation P2IA (indentation in presence of the groove) represents the near surface concentration, showing very high strain near the surface and almost zero strain below $0.5y/w$ ($\approx$ 2 x asperity half-width). P2TN (translation in the absence of asperity) represents the subsurface concentration with the maximum strain at a depth of $\approx$ $0.75y/w$. The sub surface concentration is the effect of the translation motion of the counterface (it is not seen in the calculation with no translation (P2IA)). Calculation P2TA (translation in the presence of the groove) shows both the near and the subsurface concentrations of strain. Figures 18, 19 and 20 show the residual plastic shear (in plane), circumferential and radial strain distributions, respectively. The effect of the groove vanishes at a depth $y/w > 1.0$. The in plane shear residual strain is higher in magnitude in the presence of the groove (P2TA) as compared to the case when the groove is not present (P2TN). The circumferential and radial plastic residual strains become less compressive and more tensile due to the presence of the groove. This would facilitate the nucleation and propagation of cracks in the radial and circumferential directions. Figure 21 describes the variation of the half equivalent plastic strain increment[2] ($\Delta\epsilon^p_{eq}/2$) with depth during the second cycle. This strain is generated by each successive contact and leads to the accumulation of damage and fatigue. The near and sub surface concentrations of strain are evident. The near surface concentration produced by the 7 μm deep groove extends to a

[2]this corresponds with what is normally considered the plastic strain range of the cycle.

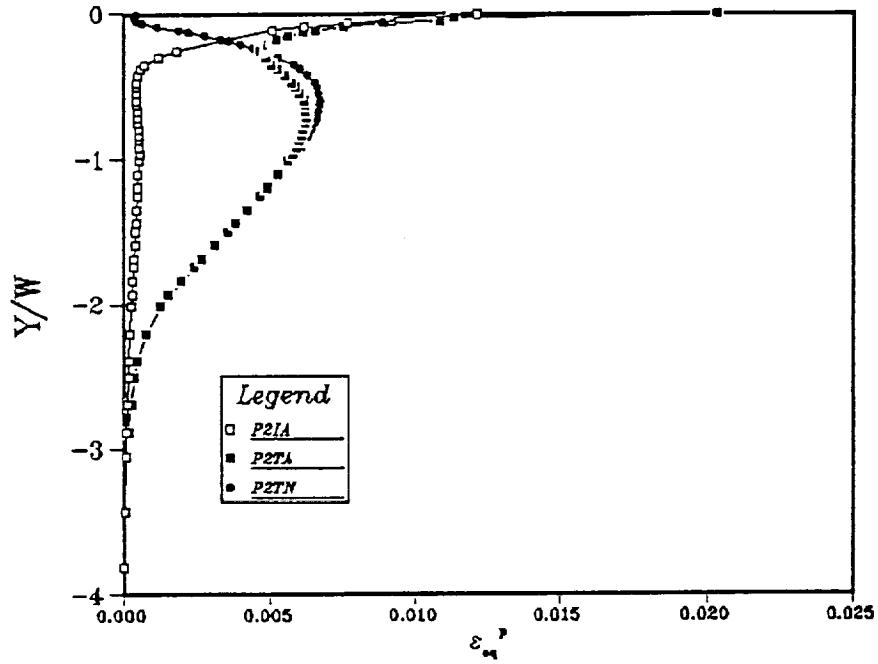

Figure 17 Variation of the accumulated plastic equivalent strain, ϵ^{p}_{eq}, with normalized depth, y/w, after 2 contacts.

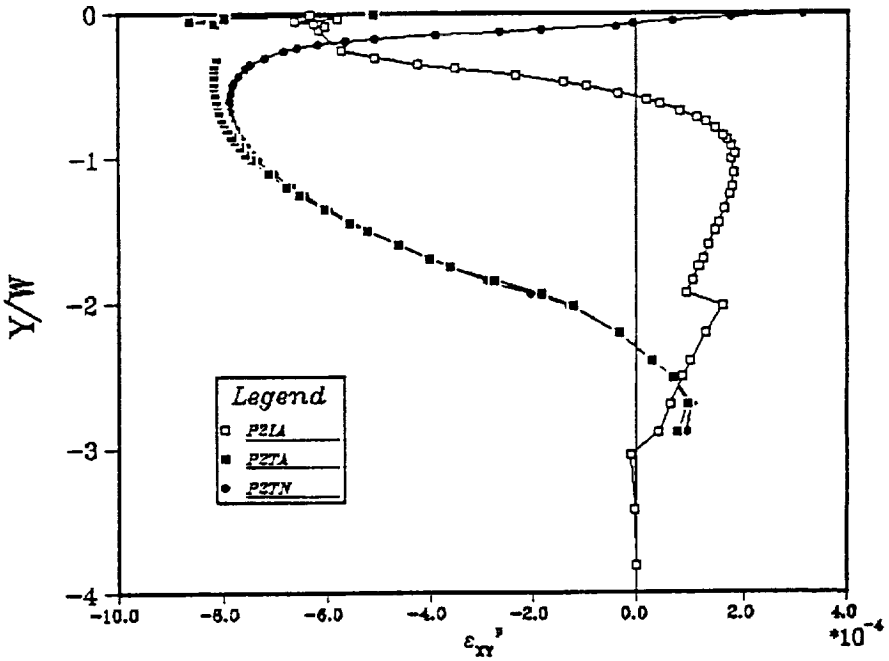

Figure 18 Variation of the residual shear plastic strain, γ_{xy}, with normalized depth, y/w, after 2 contacts.

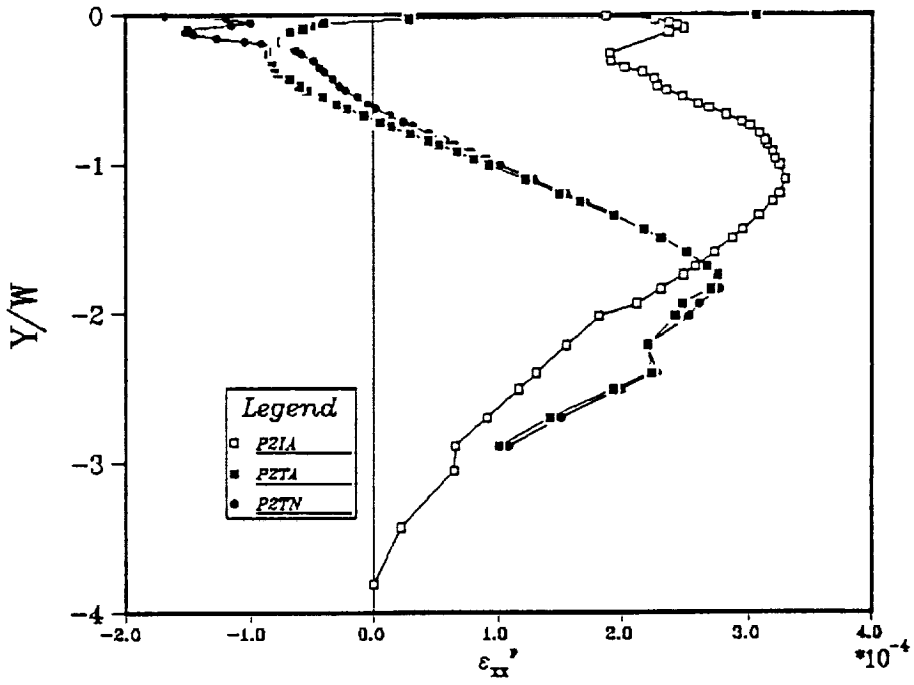

Figure 19 Variation of residual cirumferential plastic strain, ϵ_{xx} with normalized depth, y/w, after 2 contacts (model 2).

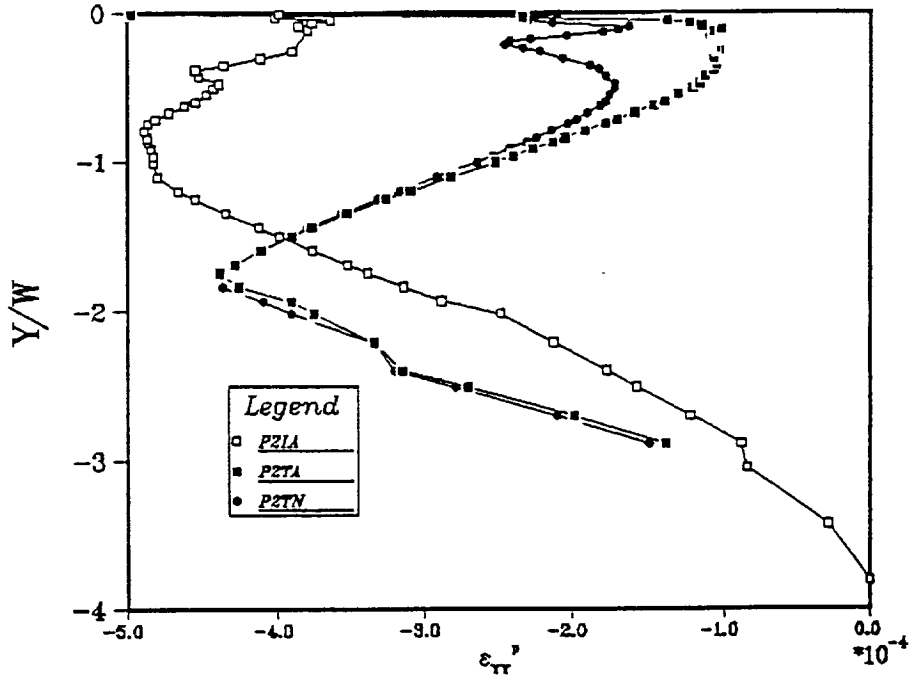

Figure 20 Variation of residual radial plastic strain, ϵ^p_{yy}, with normalized depth, y/w, after 2 contacts (model 2)

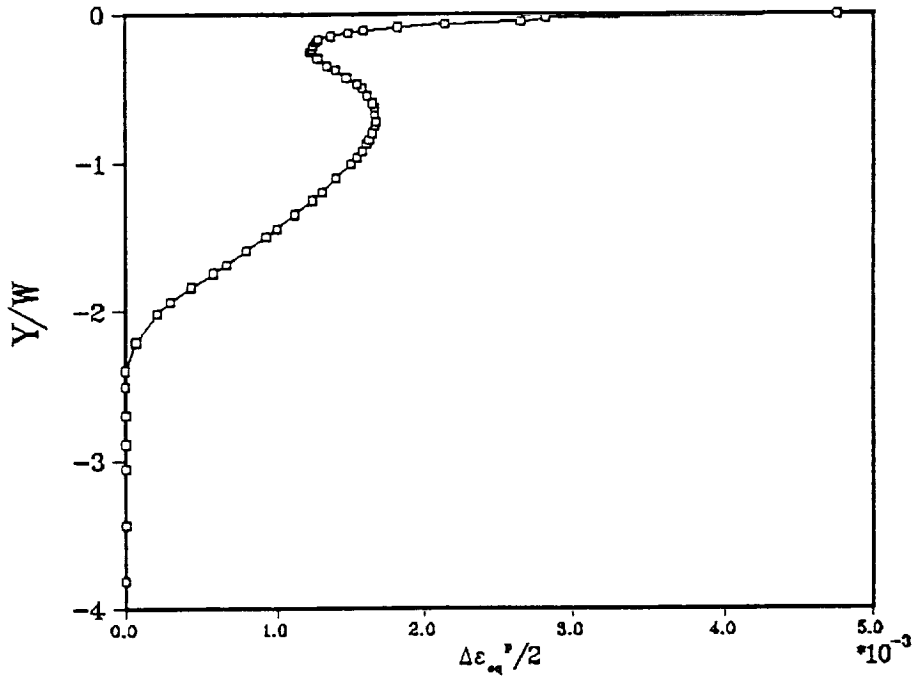

Figure 21 Variation of the half equivalent plastic strain increment, $\Delta\epsilon^p/2$, with normalized depth, y/w, for the second cycle (model 2).

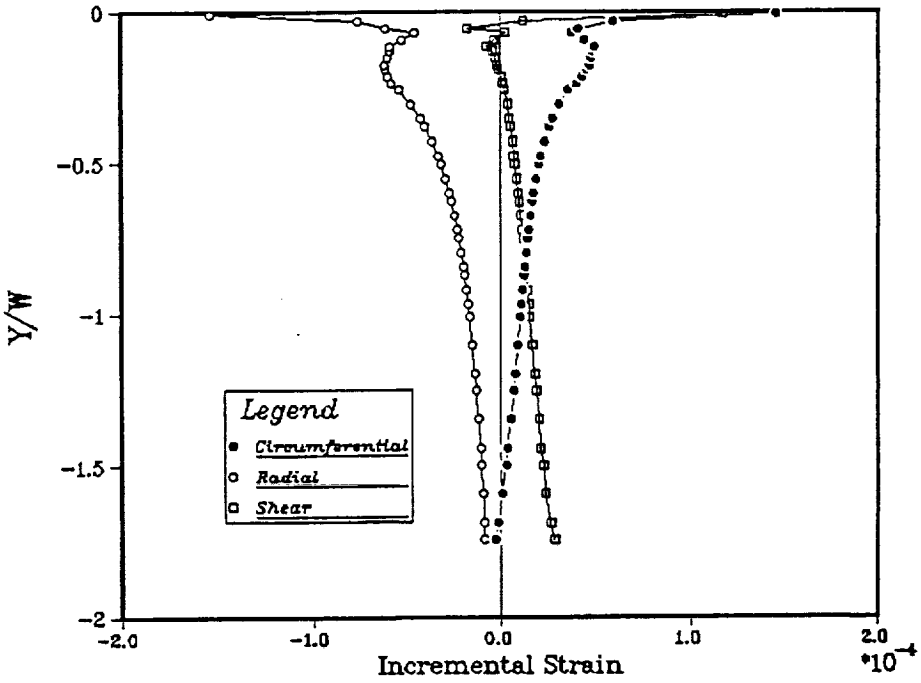

Figure 22 Incremental circumferential, radial and shear strain distribution with normalized depth, y/w, for the second cycle (model 2).

depth of about 0.3 y/w ($\approx$ 60 μm). Figure 22 shows the continuing, incremental plastic circumferential and shear strains during the second cycle. All the results are calculated below the right shoulder of the indent. Notice that the stress and strain values for P2IA and P2TA are similar near to the surface (y/w < 0.2) but are significantly different below that level, being much lower for the calculation with indentation and no translation (P2IA).

Figure 23(a) shows the half equivalent plastic strain increment contours for a part of the mesh near the asperity. Figure 23(b) shows the magnified view of the same plot. The local, near-surface strain should be compared with the peak sub surface value, $\Delta\epsilon^{p}_{eq}/2$ = 1.75×10^{-03} generated at a relative depth of y/w = 0.7. This value is exceeded close to the surface at relative depths of y/w < 0.05. These figures also show that the plasticity is higher near the left shoulder of the indent.

Figures 24 and 25 show the calculated normalized pressure distribution produced by indenting (P2IA) and translation (P2TA) after the second contact for the grooved surface and compare these with the smooth surface, Hertzian distribution. The pressure spikes produced by the groove by indentation and translation look almost identical. Figures 26 and 27 show the residual deformed configuration of a part of the half-space for calculations P2IA and P2TA. The deformation near the indent region is comparable for the two calculations. Notice that the deformation produced by indentation (P2IA) is symmetric, whereas a little asymmetry is seen in the deformed mesh after translation (P2TA).

(b) Effect of Rolling Contact with Frictional Sliding (ELKP Material)

Results were also obtained for rolling-plus-sliding in the breaking mode (for the

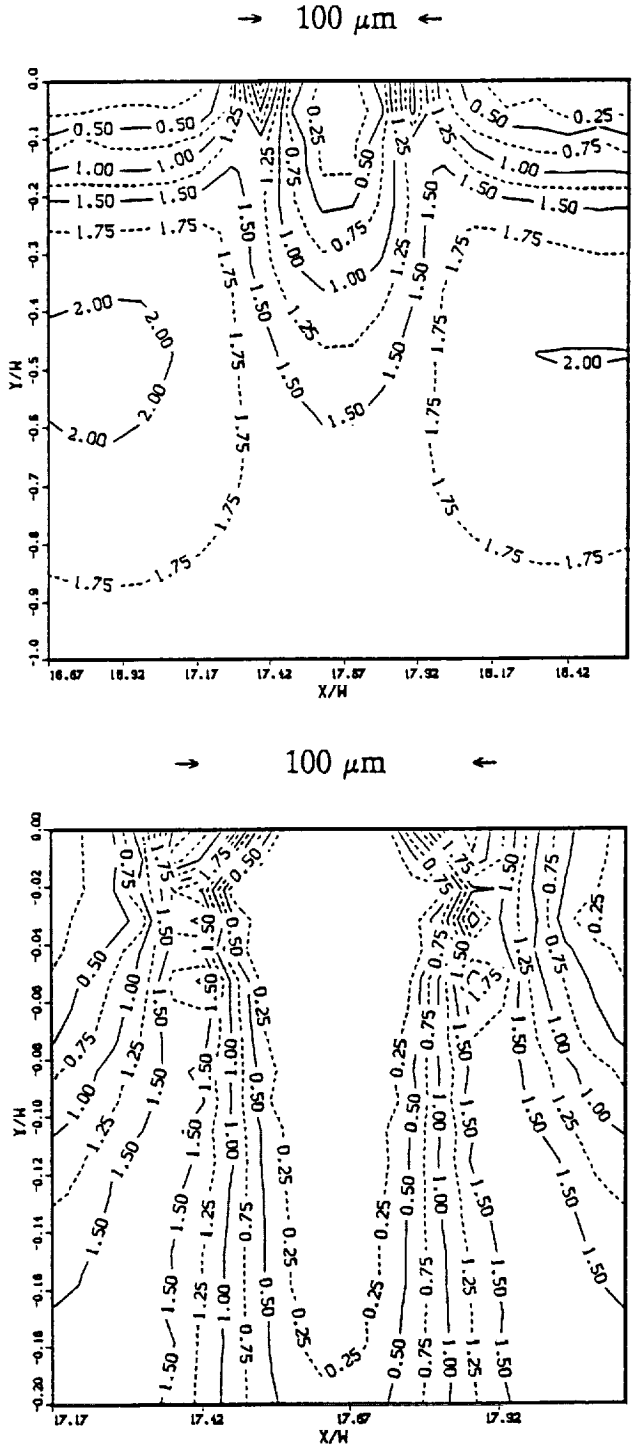

Figure 23 (a) Half equivalent plastic strain increment ($\Delta\epsilon^{p}_{eq}/2 \times 10^{03}$) contours for a small part of the mesh near the indent for the second cycle (b) magnified view of (a), showing slightly higher plasticity near the left shoulder. Rolling direction is from left to right.

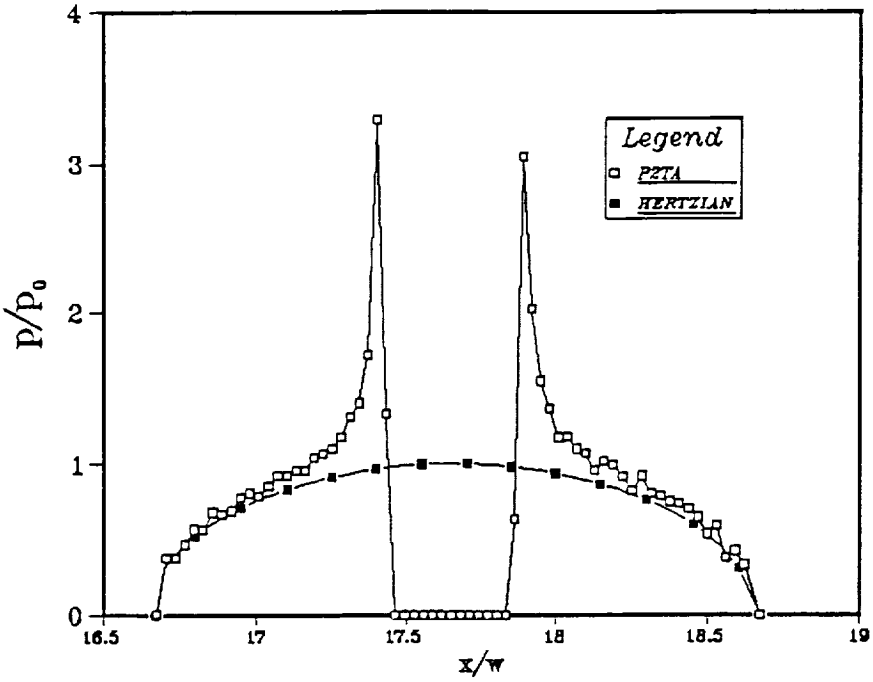

Figure 24 Normalized pressure distribution at the surface during second translation (P2TA). The center of the counterface is located at the center of the asperity.

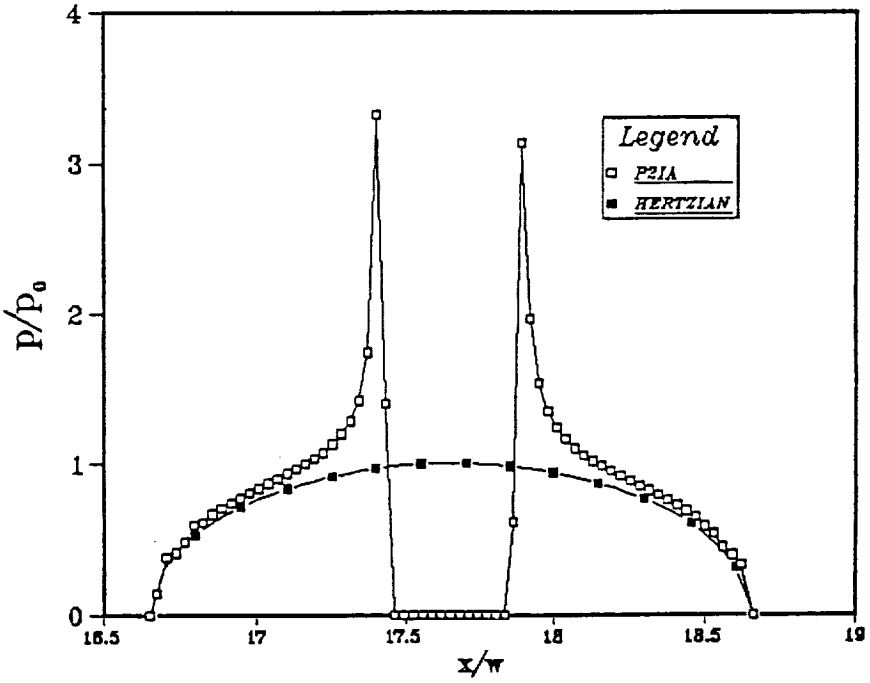

Figure 25 Normalized pressure distribution at the surface for second indentation (P2IA). The center of the counterface is right at the center of the asperity.

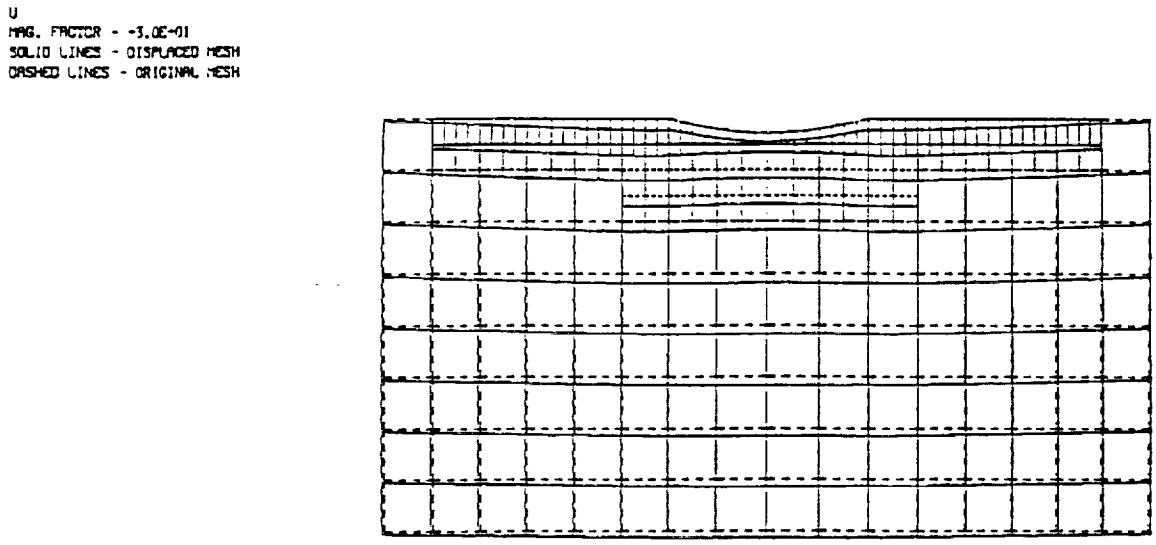

Figure 26 Deformed configuration of a small part of the half space after the second pass (residual). For calculation P2IA (indentation only).

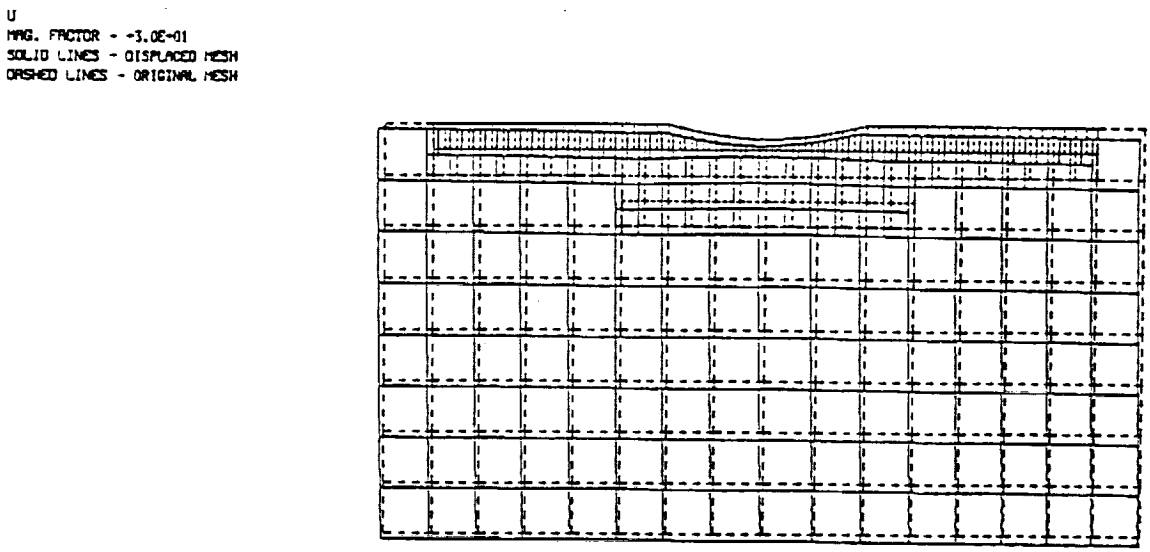

Figure 27 Deformed configuration of a small part of the half space near the indent after second pass (residual) for calculation P2TA (translation).

grooved surface) with a coefficient of friction of $\mu = 0.1$ (P2TF). These are compared with the previous results for frictionless rolling (P2TA). Figure 28 compares the normalized residual circumferential stress for the friction and frictionless case. The effect of friction is seen very near the surface but it vanishes below a depth of 0.1 y/w. Figure 29 shows the variation of circumferential strain with depth. The effect of friction is negligible near the surface. It is higher in the subsurface region and extends to a depth of $\approx$ 2y/w.

(c) Results for NLKP Material

Two indentations of the grooved surface were made for non-linear-kinematic-hardening-plastic material constitutive relations (see Appendix B). The non-linear behavior produces larger transient deformation in the first few cycles than the ELKP behavior. Figure 30 shows the deformed mesh after the second contact. This may be compared with figure 26 for ELKP behavior (noting the difference in magnification of the displacements). The larger net-deformation produces a noticeable flattening of the edges of the groove, and a corresponding 40% reduction in the intensity of the pressure spikes (compare Figure 24 and 31). Also notice a little filling out of the groove causing a reduction in the diameter of the groove. This has been experimentally seen earlier (Figure 1) by Bastias, et al. (1992). The larger net deformation also produces ~ 10x larger residual stresses near the surface as is evident from the comparison of Figures 15 and 32. Distributions are jagged near the surface indicating a possible lack of refinement of the mesh for such high amounts of deformation. Evidence of tensile stresses near the surface are also found elsewhere in the literature. Muro, et al. (1973) have measured residual stresses using X - ray techniques. They

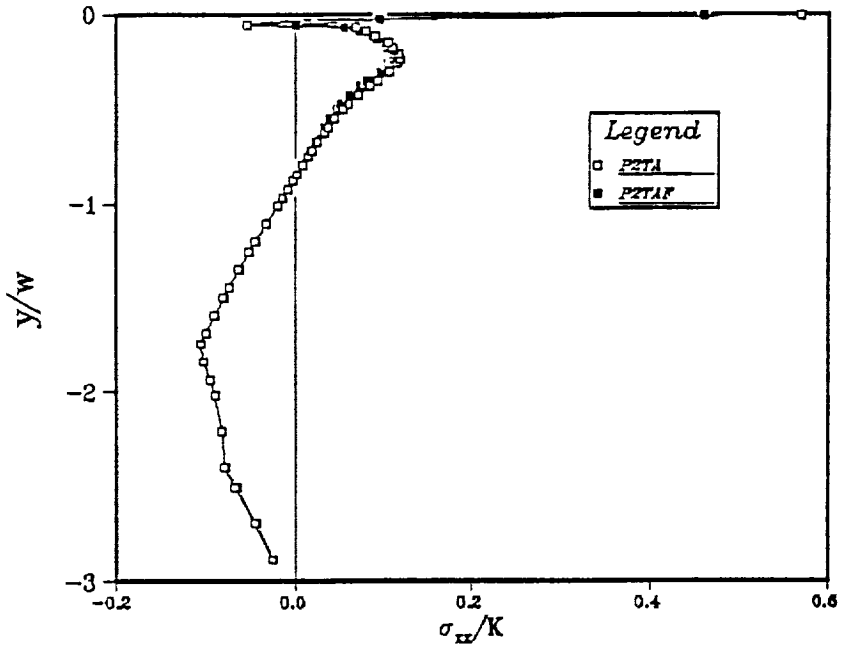

Figure 28 Normalized residual circumferential stress as a function of normalized depth, y/w, for calculations P2TF (translation with friction) and P2TA (translation without friction).

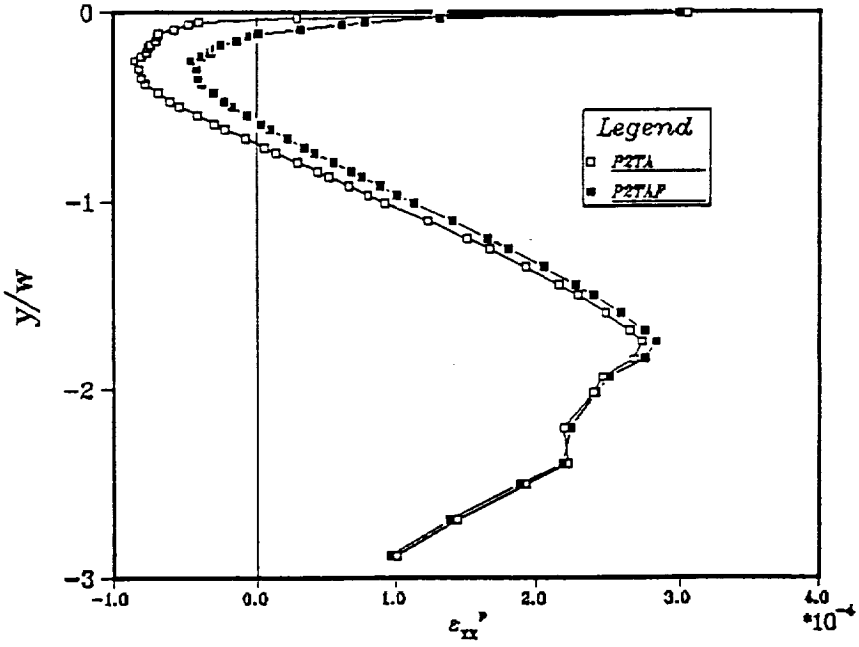

Figure 29 Circumferential residual plastic strain, ϵ_{xx}^{p}, as a function of normalized depth, y/w, for calculation P2TF (translation with friction) and P2TA (translation without friction).

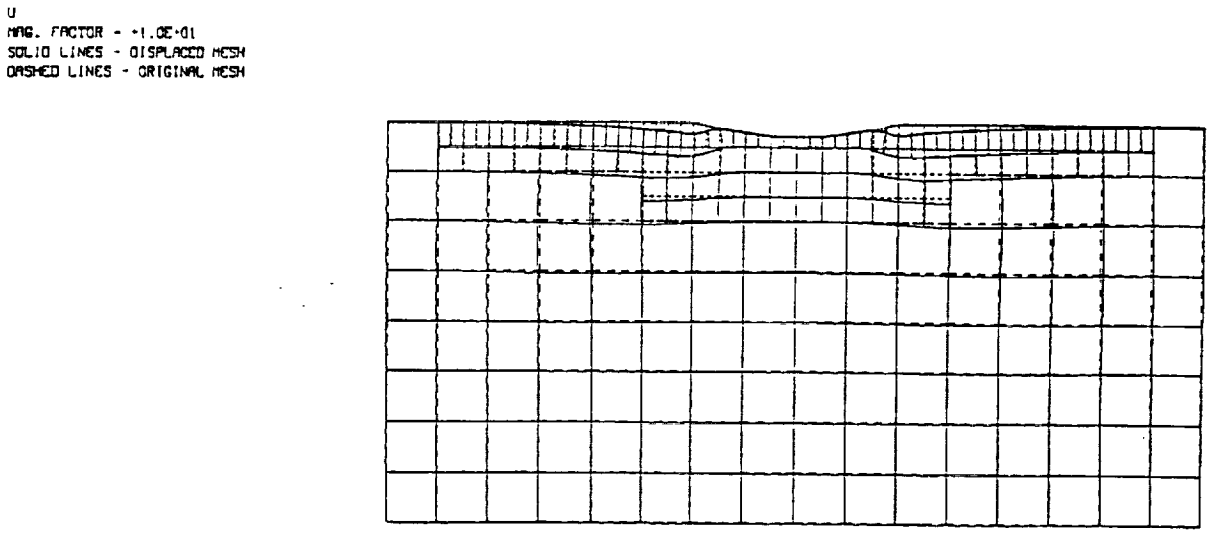

Figure 30 Deformed configuration of a small portion of the half space after the second pass (residual) for the calculation NL2IA.

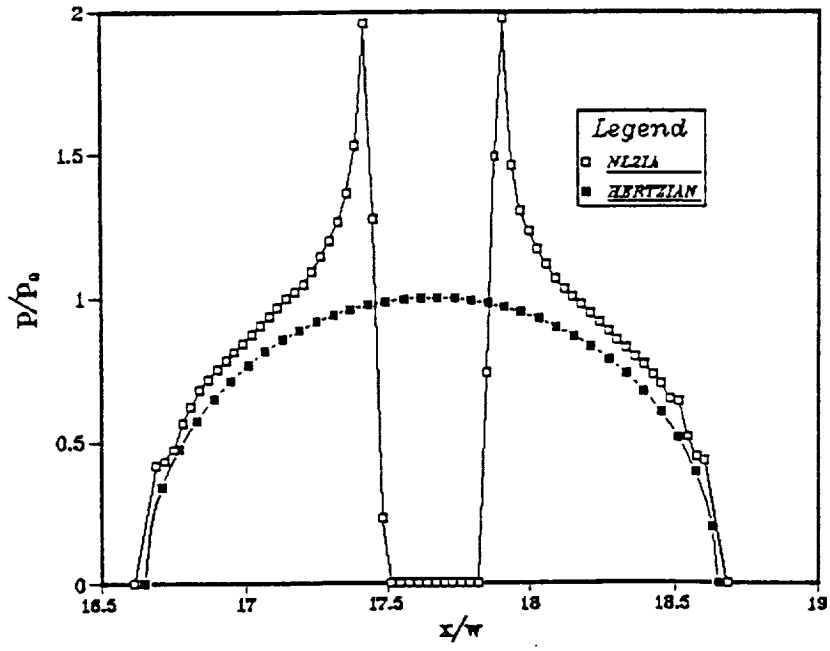

Figure 31 Normalized pressure distribution at the surface, half way through the second pass for calculation NL2IA.

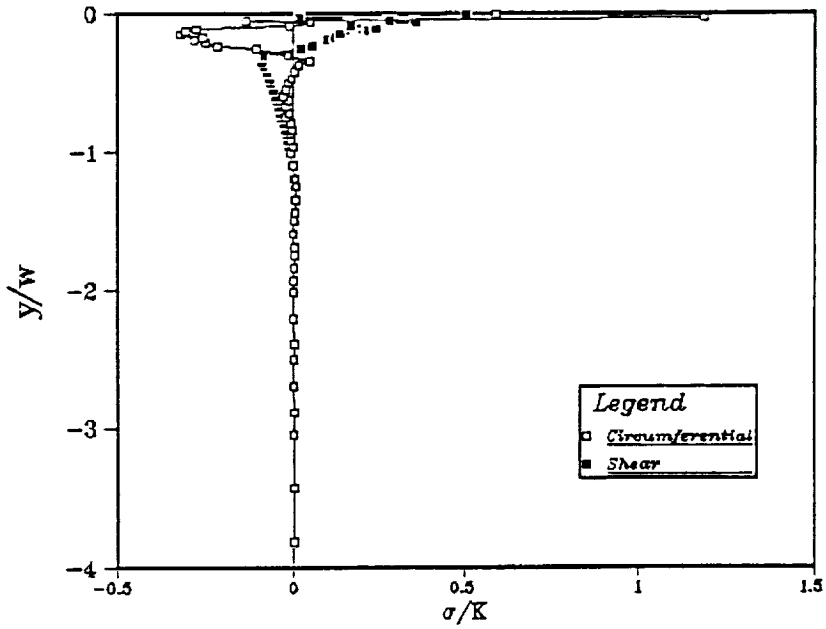

Figure 32 Residual circumferential and shear stress distribution with normalized depth for calculation NL2IA (indentation in the presence of asperity for NLKP properties)

have reported a tensile circumferential stress of 900 MPa in roller bearings for a peak pressure of 6.5 GPa. Voskamp (1980) and Zaretsky (1969) have also reported residual tensile stresses near to the surface for bearing steels.

3.2 Comparison of Finite Element Results with Experimental Measurements

The profile measurements of the artificially placed indents on 440C steel samples are compared with the finite element calculations for the same material. The profile of the indent is measured running the profilometer parallel to the axis of the cylindrical rod shaped samples, before and after rolling. The residual deformation measured is compared with that calculated using the finite element model (model 2). Figure 33 shows the profilometer traces (a) just after the groove has been made on the already present running track and (b) after

rolling over the freshly made groove for 3 minutes ($\approx$ 10000 cycles) at a peak pressure of 4.85 GPa. Figure 34 shows the superposed view of figure 33(a) and (b). Figure 34 was created by manually digitizing the traces in Figure 33 and then superposing them. The peak deformation at the indent shoulder is about 2.3 μm. This result is compared to the finite element calculation, P1IAS, where the shoulders at the corners of the indent have been introduced in the finite element mesh. This calculation produces a peak residual deformation of 1.95 μm at the shoulder. Calculation NL1IAS (NLKP material properties, shoulders introduced in the mesh), produces a peak deformation of 0.7 μm at the shoulders. The parameters used in the subroutine 'UMAT' (see Appendix B) are applicable to 52100 steel. Figure 35(a) shows a track for a 440C steel RCF sample. This track is wider and deeper than that for 52100 steel in Figure 35(b), since 440C (HRC 55-56) is more compliant than 52100 (HRC 62-64) steel. Appropriate parameters to be used in the subroutine UMAT for 440C steel are being calculated.

Rolling contact over artificially placed indents is seen to nucleate a spall at the exit end of the indent (Lubrecht, 1990, Bastias, 1990). The reason for this has not been clear. In this study, rolling + sliding calculations were performed over the groove with the shoulders introduced at its edges. ELKP set 2 (see table 3) material properties were used with a coefficient of friction, $\mu = 0.1$. Three complete passes were made. These calculations (P1TAFS, P2TAFS and P3TAFS) are similar to P1TAF, except that the shoulders have been introduced at the edge of the groove. Figure 36 (a) shows the incremental equivalent plastic strain between cycles 2 and 3. Figure 36 (b) shows the residual Mises stress contours near the groove after the third cycle. Significantly higher values are seen near the right shoulder

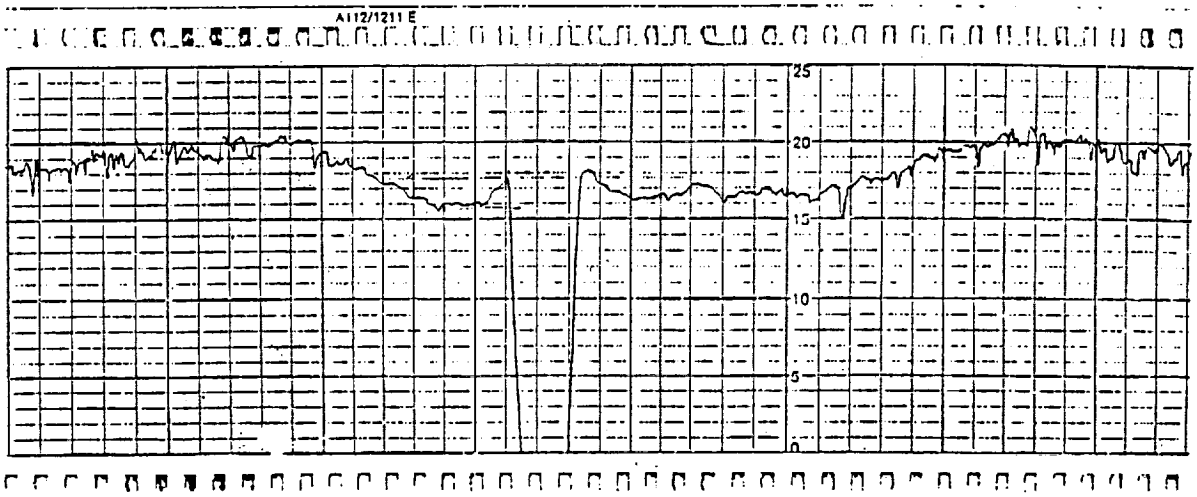

(a)

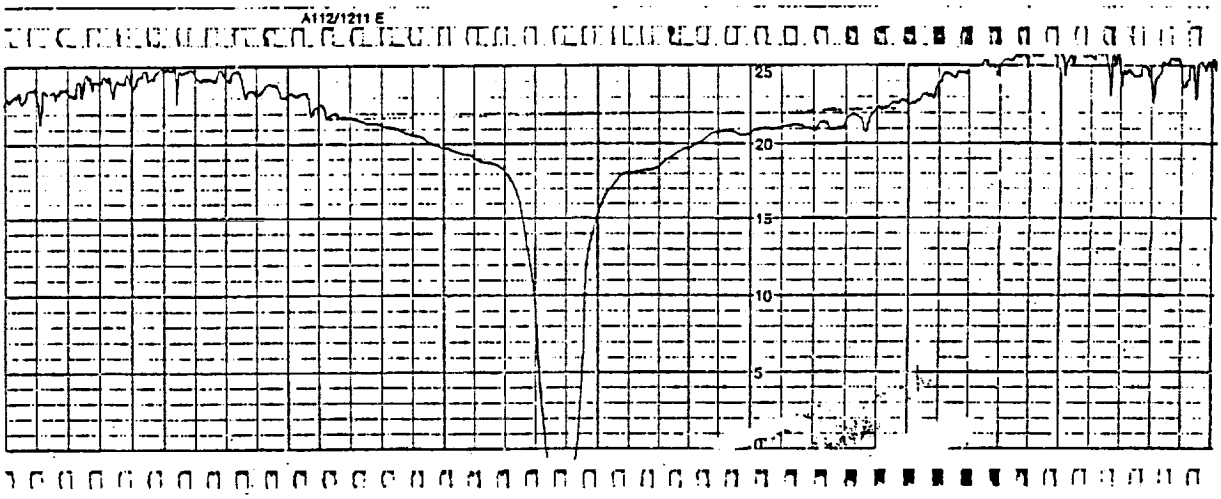

(b)

Figure 33 Profilometer trace of the groove (a) just after it is placed on the already present running track and (b) after rolling over it for 3 minutes ($\approx$ 10000 cycles). Vertical magnification = 10000, horizontal magnification = 100. Rolling direction is from left to right.

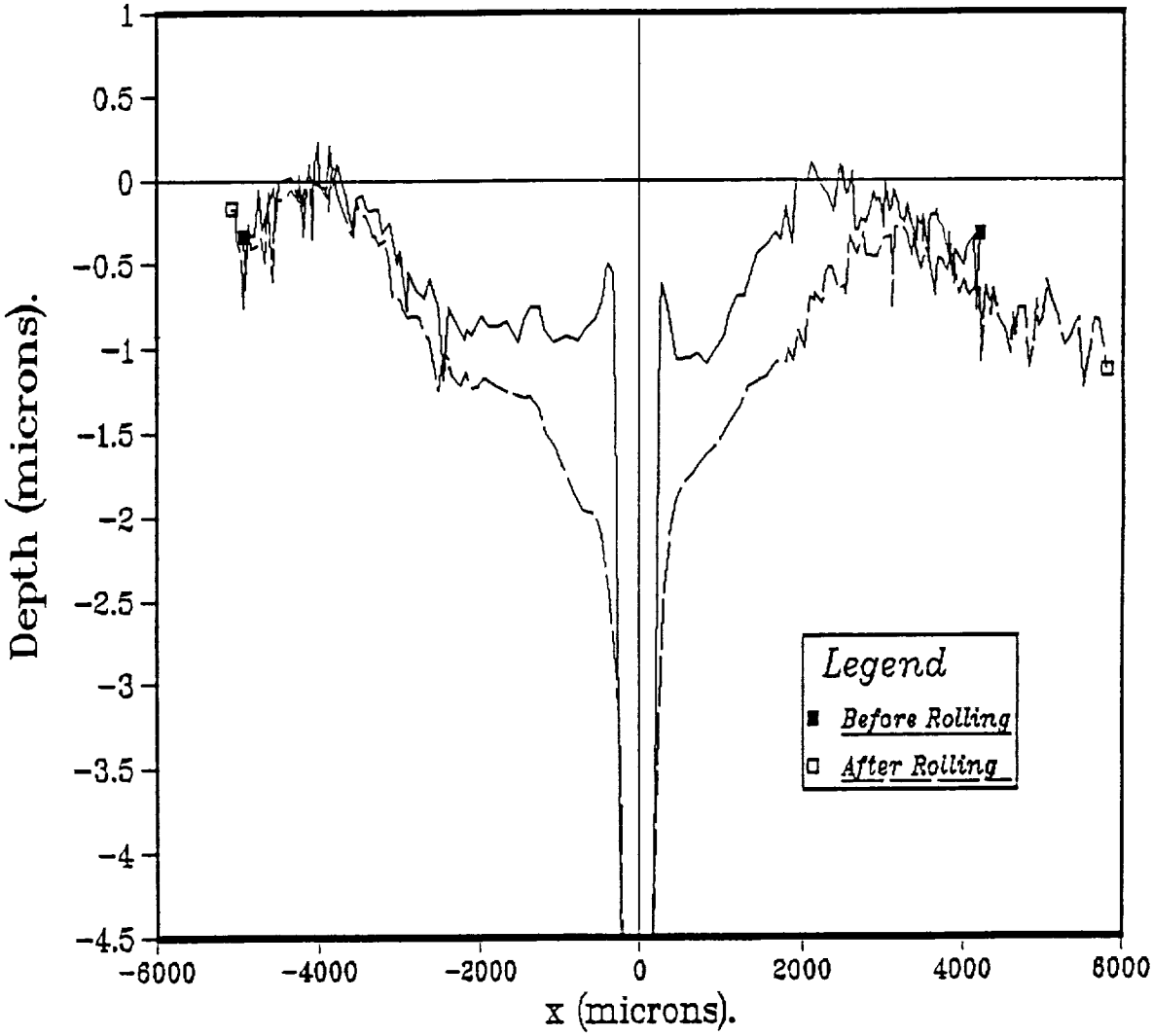

Figure 34 Superposed view of the groove profile before and after rolling for 3 minutes. The traces in fig. 33 are digitized and then superposed to obtain this plot. Rolling direction is from left to right.

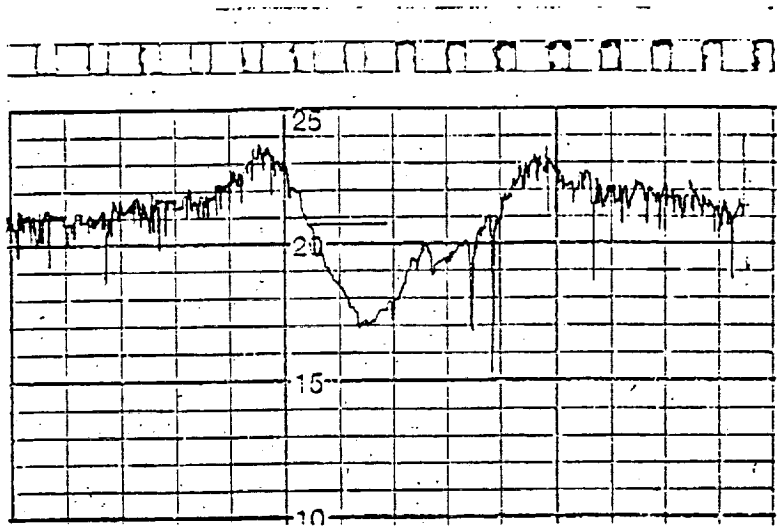

(a)

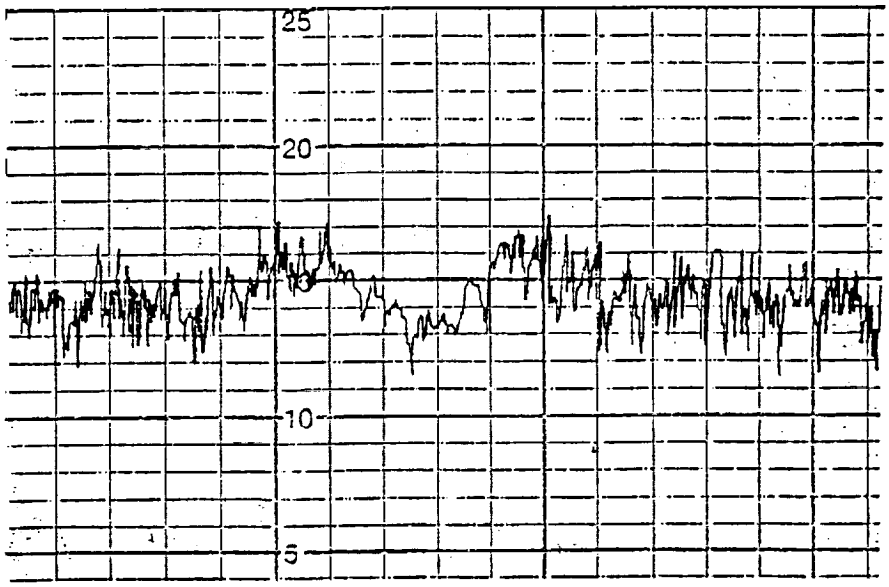

(b)

Figure 35 Profile of the running track of (a) a 440C steel RCF specimen and (b) a 52100 steel RCF specimen, after rolling over ≈ 100 cycles at a peak pressure of 4.85 GPa. Vertical magnification = 10000, Horizontal magnification = 20.

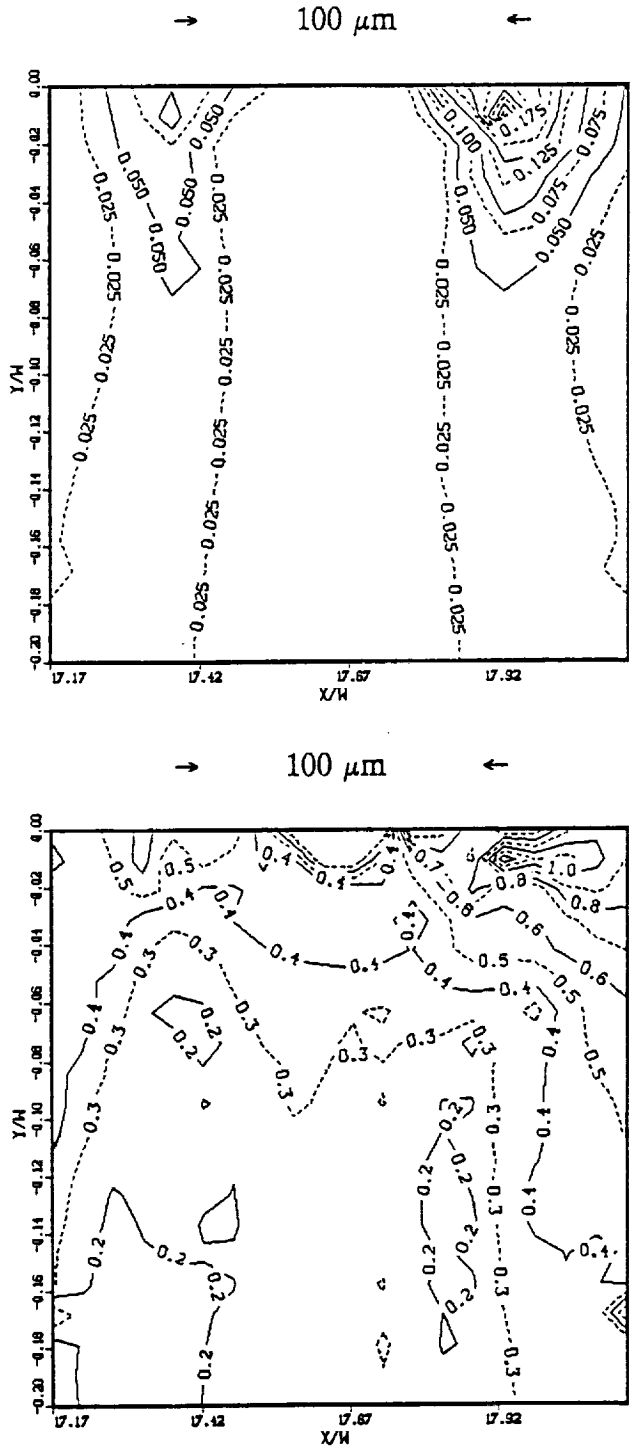

Figure 36 (a) Incremental equivalent plastic strain range ($\Delta\epsilon^{p}_{eq}/2$) contours between passes 2 and 3 and (b) residual Mises stress (GPa) contours after the third pass for a small part of the mesh near the groove. Rolling direction is from left to right.

as compared to the left shoulder. The plasticity and stress values are so much higher near the right shoulder (upto 50%) that spall nucleation, as seen in experiments (see Figure 1), will almost certainly occur in the vicinity of the right shoulder.

3.3 Effects of plastic deformation of the asperity

Large plastic deformation occurs at the corners of a freshly introduced asperity in the initial few rolling contacts (see Figure 34). The asperity achieves a steady state shape after as few as 15000 contacts. Finite element calculations have been made after introducing the deformed shape of the asperity in the mesh. A single indentation of the half-space was made. Figure 37 shows the normalized pressure distribution at the surface. The peak p/p_0 decreases from 3.3 (in case of undeformed asperity, Figure 24) to 2.4 in this case. The peak stresses and strains are also found to be lower by about 30 percent. Thus the very intense pressure spikes produced by a newly formed asperity are quickly diminished by plastic deformation.

4. Discussion

The elastic finite element results for dry rolling contact on a 0.4 μm groove (model 1), compare fairly well with published results for EHD lubricated contact (Elsharkawy and Hamrock, 1991). The pressure spikes calculated by the elastic finite element model are more intense than those reported for EHD (elasto-hydrodynamic) lubricated contact. This is consistent with the absence of the thin lubrication film which supports pressure over the groove. Elasto-plastic finite element calculations show that the plastic deformation of the

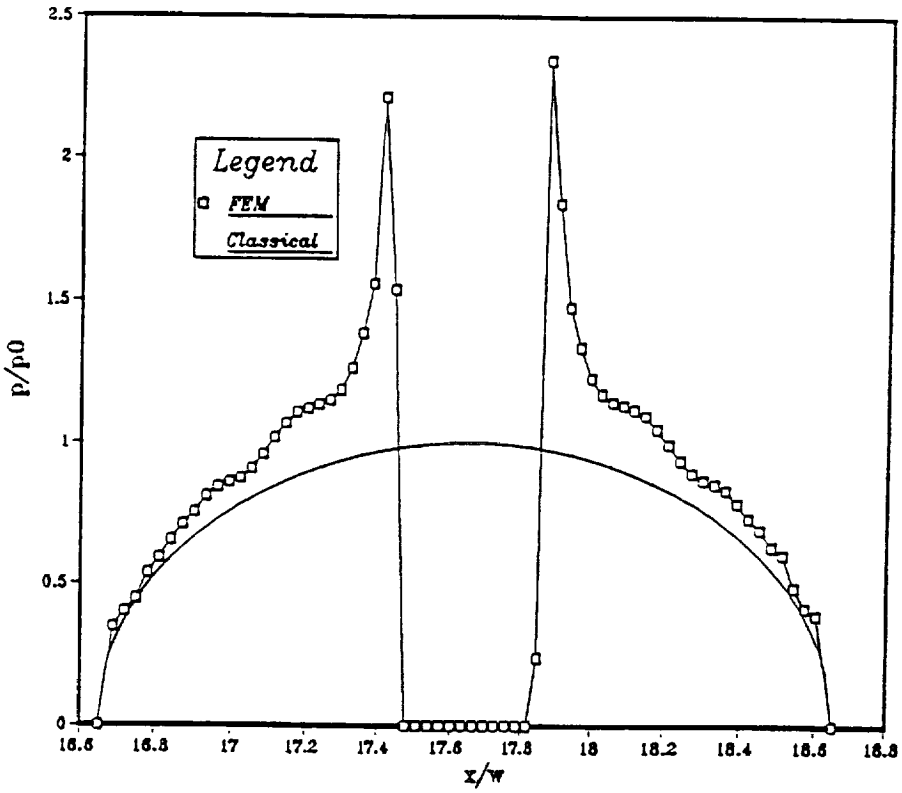

Figure 37 Normalized pressure distribution at the surface for the indentation of the asperity with the steady state shape obtained after plastic deformation.

groove considerably modifies the pressure spikes and the strain distribution (Figure 9). After plastic deformation, the calculated pressure spikes are less intense than those reported for the EHD contact (compare Figures 8 and 9). Thus, the effect of plastic deformation on the spikes may outweigh that of a thin lubrication film.

Calculations for the deep indent (model 2) reveal some interesting features. The pressure distributions, stresses and strains and residual deformations produced near the surface by indenting the groove are very similar to those obtained by rolling. It appears that the near-surface effects of surface irregularities subject to repeated rolling contact can be simulated by repeated indentation. Although, the stress and strain distributions in the subsurface are quite different for rolling (translation) and indentation (no translation).

The presence of the groove greatly increases the magnitude of near surface stresses and strains. So much so, that they exceed the peak subsurface values (Figures 16, 17 and 18). Thus, the values near the surface rather than those in the subsurface become critical for spall nucleation. These near surface values can be closely approximated by values calculated from repeated indentations. This observation may prove very useful in developing a 3-D "two-body" model. A model for indentation of a half-space by a cylinder would be much smaller and simpler than one required to simulate rolling. This may save a considerable amount of "computer time" which is a critical constraint in developing a 3-D model. For the 2-D model, indentation consumes 1/5 th of the computer time as opposed to a complete translation of the counterface over the half-space. Also, it is noticed that the effect of asperity does not extend below a depth of 1.0 y/w = 2 x asperity width, consistent with "Saint Venant's principle" (Figures 15 to 20).

Calculations simulating rolling show that incremental plasticity is slightly different at the two edges of the groove (Figure 23). But when shoulders $\approx$ 1 μm in height are added at the edges of the groove and rolling + sliding calculations performed, the incremental plasticity and residual stresses are found to be significantly higher at the right shoulder. This might explain the nucleation of spalls preferentially at the exit end of artificial indents, as observed by Lubrecht (1990) and Bastias (1990). This suggests that the shoulders at the edges of the irregularities may play an important role in the nucleation of cracks. More study is required to offer a fuller explanation.

The effect of friction on the magnitude and distribution of stresses and strains, for a coefficient of friction μ = 0.1, appears to be small. Thus, the mechanical effect of friction is found to be negligible for conditions of lubricated rolling contact. But thermal effects for even small coefficients of friction can be considerable for poorly cooled bearings. High residual tensile stresses are generated (Gupta, 1991). The effect is accentuated by the temperature dependence of the material and thermo-physical properties.

Shoulders developed at the edge of the indents (see Figure 33) placed on the RCF samples are seen to deform considerably as they are rolled over. This deformation compares well with the deformation predicted from the finite element calculations (sec. 3.2). Experiments indicate that the deformed shape of the indent quickly reaches a steady state ($\approx$ 15000 cycles). Calculations performed by inserting this steady state shape in the finite element model shows that the pressure spikes are lower by as much as 30 percent compared to the undeformed shape.

CONCLUSIONS

1. Finite element results for dry elastic contact, using a "two-body" model, compare well with published results for EHD lubricated contact. The effect of plastic deformation may overweigh the effect of presence of the lubricant film.

2. Repeated rolling contact can be closely approximated by repeated indentations for the results near the surface in presence of an asperity.

3. The presence of an asperity greatly increases the magnitude of the stresses and strains. It introduces a near surface concentration of stresses and strains with peaks higher than the sub-surface concentration. This promotes the near surface failure mode.

4. The effect of asperity extends to a maximum depth of 1.0 y/w = 2 x asperity width.

5. The shoulders at the edge of the irregularities considerably modify the stresses and strains near the surface and hence may play a important role in crack nucleation. The plasticity and residual stresses are found to be higher at the exit end of the groove where the spalls are seen to nucleate in experiments.

6. The mechanical effect of friction for low coefficients of friction $\approx$ 0.1 (as seen in lubricated contacts), is negligible.

7. The residual deformation of the artificial indents planted on RCF samples, measured using a profilometer, compare very well with the residual deformations calculated from the finite element model.

8. Severe plastic deformation of the indent occurs. This deformation considerably reduces the intensity of the pressure spikes.

FUTURE WORK

1. Calculations for several dent shape and sizes, and peak pressure will be performed. The parameters which determine the depth, position and amount of peak plasticity will be identified.

2. Even the most recent life prediction models in rolling contact rely on elastic solutions to determine the sub surface distribution of stresses and strains. Further, most of them do not treat the effect of the presence of defects such as those in this study. Therefore the stress and strain distributions obtained from these finite element models will be used to modify the existing life prediction theories. These predictions will be compared to the RCF experiments being performed under the current study.

3. The various parameters for the user subroutine 'UMAT' (see Appendix C), for 440C steel will be calculated. This subroutine encodes the non-linear-kinematic-hardening-plastic (NLKP) material constitutive relations, described by McDowell (1985). These constitutive relations are expected to be more suitable for modelling the plastic deformation

4. Rolling contact fatigue experiments with different shapes and sizes of the artificial dent and different peak pressures will be performed. These results along with the analytical results from the finite element calculations will be used to identify correlations between the various parameters affecting the life of the RCF samples. Also these results will be used to make comparisons with the analytical life predictions.

5. With the profilometer interfaced to the computer, 3-D profiles of the indents and the spalls will be studied. Efforts to develop a three dimensional, two-body finite element model' will be made. These studies will provide a better understanding of the mechanism

of spall formation. Further, the stress and strain distributions obtained using the model will be used in the life prediction models.

ACKNOWLEDGEMENTS

The authors would like to thank Hibbitt, Karlsson and Sorensen, Inc. for permission to use their excellent finite element code 'ABAQUS'. The calculations were conducted on the CRAY-2 at the National Center for Supercomputer Applications (NCSA) at the University of Illinois at Urbana-Champaign. The rolling experiments were performed in a ball/rod testing machine designed, and provided by NTN-Bower Corp. Thanks are due to Mr. Larry Besk of the Rank Taylor Hobson, for his kind advice in interfacing of the Talysurf to the computer.

REFERENCES

Bastias, P.C., Hahn, G.T., Gupta, V., Rubin, C.A. and Leng, X., 1992, "Analysis of Rolling Contact Spall Life in 440C Bearing Steel", presented at the *1992 Conference on Advanced Earth-To-Orbit Propulsion Technology* at the NASA/George C. Marshall Space Flight Center, Huntsville, Al.

Bastias, P.C., Gupta, V., Leng, X., Rubin, C.A. and Hahn, G.T., 1991, "Nucleation and Growth of Rolling Contact Failure of 440C Bearing Steel", *Quarterly Report to NASA-MSFC, September 1991.*

Bastias, P.C., Du, J., Hahn, G.T., and Rubin, C.A., 1990, "Analysis of Rolling Contact Spall Life in 440C Steel Bearing Rims", *Final Report to NASA-MSFC (NAS8-37764).*

Bhargava, V., Hahn, G.T., and Rubin, C.A., 1990, "Rolling Contact Deformation, Etching Effects and Failure of High Strength Bearing Steels", *Met. Trans. A.*, Vol. 21A, pp. 1921-1931.

Bhat, B.N. and Dolan, F.J., 1982, "Past Performance Analysis of HPOTP Bearings", *NASA TM-82470.*

de Mul, J.M., Vree, J.M., and Kuypers, J.C., 1987, "The influence of certain Raceway Dent Geometries (3-D) on Contact Stresses and Rating Fatigue Life of Rolling Bearings", *Journal of Tribology*, Vol. 109, pp. 452-461, July 1987.

Elsharkawy, A.A., and Hamrock, B.J., 1990, "Subsurface Stresses in Micro EHL Line Contacts", *Joint ASME/STLE Tribology Conference,* Paper No. 90-Trib-11, Toronto, Canada, October 7-10, 1990.

Glover, D., "A Ball-Rod Rolling Contact Fatigue Tester",*ASTM STP 771,* J.J.C. Hoo, Ed., pp. 107-124.

Gupta, V., Bastias, P.C., Rubin, C.A. and Hahn, G.T., 1992, "Nucleation and Growth of Rolling Contact Failure of 440C Bearing Steel", Quarterly Report to NASA-MSFC, January 20, 1992.

Gupta, V., Bastias, P.C., Hahn, G.T. and Rubin, C.A., 1991, "Elasto-Plastic Finite Element Analysis of 2-D Rolling Plus Sliding Contact with Temperature Dependent Bearing Steel Material Properties", Presented at the *Army Symposium for Solid Mechanics,* Plymouth, M.A., 1991.

Hahn, G.T., Bhargava, V., Chen, Q. and Kim, K.Y., "The Cyclic Stress-Strain Properties, Hysterisis Loop Shape and Kinematic Hardening of a Rail Steel",

Metallurgical Transactions A., To be published.

Kumar, A.M., Kulkarni, S.M., Bhargava, V., Hahn, G.T. and Rubin, C.A., 1987, "Mechanisms of Rolling Contact Spalling of 440C Steel", *Final Report to NASA-MSFC (NAS8-36651).*

Leng, X., 1990, "Elasto-Plastic Finite Element Analysis of Repeated Rolling Contact Between Two Deforming Bodies", Master Thesis, Materials Science and Engineering Department, *Vanderbilt University.*

Lubrecht, A.A., Venner, C.H., Lane, S., Jacobson, B. and Ionnides, E., 1990, "Surface Damage, Comparison of Theoretical and Experimental Endurance Lives of Rolling Bearings", *Proceedings of the Japan International Tribology Conference, 1990.*

McDowell, D.L., 1985, "A Two Surface Theory for Non-Proportional Cyclic Plasticity, Part 1: Development of Appropriate Equations", *Journal of Applied Mechanics*, 1985, Vol. 52, pp. 298-302.

McDowell, D.L., 1985, "A Two Surface Theory for Non-Proportional Cyclic Plasticity, Part 2: Comparison of Theory with Experiments", *Journal of Applied Mechanics*, 1985, Vol. 52, pp. 303-308.

McDowell, D.L., Bhargava, V. and Hahn, G.T., "The Cyclic Flow Properties of a 1050 Steel and the Effect of Strain Rate", *Unpublished research.*

Muro, H., Tsushima, N., and Nunome, K., 1973, "Failure Analysis of Rolling Bearings by X-Ray Measurement of Residual Stress", *Wear, 25 (1973) 345-356.*

Sayles, R.S. and Ioannides, E., 1988, "Debris Damage in Rolling Bearings and its Effects on Fatigue Life", *Journal of Tribology,* Vol. 110, pp. 26-31, Jan. 1988.

Shao, E., Huang, X., Wang, C. and Chen, Q., 1987, "A Method of Detecting Rolling Contact Initiation and Establishment of Crack Propagation Curves", *ASLE Reprint 87-AM-4E.*

Venner, C.H., Lubrecht, A.A., and ten Naple, W.E., 1990, "Numerical Simulation of the Overrolling of a Surface Feature in an EHL Line Contact", *Journal of Tribology,* Vol. 113, October 1991, pp. 777-783, Transactions of the ASME.

Voskamp, A.P., Osterlund, R., Becker, P.C., and Vingsbo, O., 1980, "Gradual Changes in Residual Stress and Microstructure during Contact Fatigue in Ball Bearings", *Metals Technology*, January 1980, pp. 14-21.

Webster, M.N., and Sayles, R.S., 1986, "A Numerical Model for the Elastic Frictionless Contact of Real Rough Surfaces", *Journal of Tribology,* Vol. 108, pp. 314-320, Jul. 1986.

Zaretsky, E.V., Parker, R.J. and Anderson, W.J., 1969, "A Study of Residual Stress Induced during Rolling Contact", *Journal of Lubrication Technology,* ASME Transaction (F), Vol. 91, pp. 314-319.

APPENDIX A

Rolling contact fatigue testing of cylindrical specimens with spherical balls is a three dimensional situation. The finite model developed here is for a simplified two dimensional case. This appendix derives an expression for the radius of the counterface (for the 2-D FEM calculations) which produces a contact patch equivalent to that of the three dimensional situation, maintaining the same peak pressure and material properties.

For three dimensional contact the semi-major axis, a_{3D} and semi-minor axis, b_{3D} are given by -

$$a_{3D} = \frac{4\bar{E}R_s p_o k}{E'}$$

$$b_{3D} = \frac{4\bar{E}R_s p_0}{E'}$$

where,

$$\frac{1}{R_x} = \frac{1}{R_{x1}} + \frac{1}{R_{x2}}$$

$$\frac{1}{R_y} = \frac{1}{R_{y1}} + \frac{1}{R_{y2}}$$

$$\frac{1}{R_s} = \frac{1}{R_x} + \frac{1}{R_y}$$

$$\bar{E} = 1.0003 + 0.\frac{5968}{\frac{R_y}{R_x}}$$

$$E' = 2\left[\frac{1-\nu_1^2}{E_1} + \frac{1-\nu_2^2}{E_2}\right]$$

$$k = a_{3D}/b_{3D}$$

$$P = \frac{2}{3}\pi abp_0$$

where,

P = Total load = Volume of semi-ellipsoid with semi-axis a, b and p_0.

and p_0 = peak pressure

The symbols R_{x1}, R_{x2} etc. are defined in Figure A1.

For line contact,

$$a_{2D} = \frac{4R_{2D}P_0}{E'}$$

Equating the semi minor axis of the 3D contact, b_{3d}, to the semi minor axis of the 2D contact, a_{2d}, we get -

$$R_{2D} = \bar{E}R_s$$

for our case of ball and rod RCF machine:

$R_{x1} = R_{y1}$ = 0.25 in. = ball radius.

R_{x2} = 0.375/2 in. = radius of the rod.

$R_{y2} = \infty$

therefore:

$$\bar{E}=1.25607$$

and

$$R_s=1.905x10^{-3}$$

This yields an equivalent 2D radius of 2.4 mm.

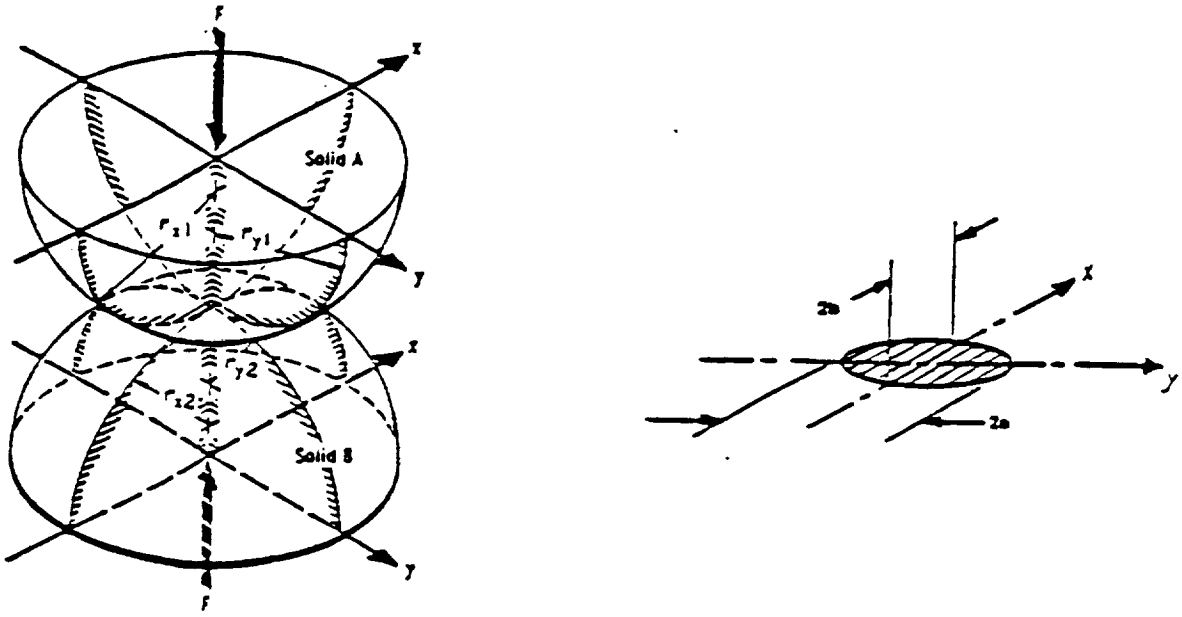

Figure A1 Geometry of contacting solids.

APPENDIX B

NON-LINEAR-KINEMATIC-HARDENING-PLASTIC (NLKP) MATERIAL BEHAVIOR

The McDowell bounding surface model (McDowell, 1985) consists of a Von-Mises type yield surface shifted by a back stress, α (see figure B1):

$$f = 3/2(\underline{s} - \underline{\alpha}) : (\underline{s}-\underline{\alpha}) - R^2$$

where,

$$\underline{s} = \underline{\sigma} - 1/3(\sigma_{kk}\underline{I})$$

The flow rule is:

$$\dot{\underline{\varepsilon}}^p = 1/h(\underline{\dot{s}}:\underline{n})\underline{n} \text{ if } f=0 \text{ and } \underline{\dot{s}}:\underline{n}>0$$

otherwise, $\dot{\underline{\varepsilon}}^p = 0$ where:

$$\underline{n} = (\underline{s}-\underline{\alpha})/ \| \underline{s}-\underline{\alpha} \|$$

The back stress $\underline{\alpha}$, is decomposed into $\underline{\alpha}^s$, the short range backstress and $\underline{\alpha}^*$ the long range backstress.

$$\underline{\alpha} = \underline{\alpha}^s + \underline{\alpha}^*$$

The evolution of the backstress is defined by:

$$\dot{\underline{\alpha}} = \dot{\underline{\alpha}}^s + \dot{\underline{\alpha}}^* \text{ where } \dot{\underline{\alpha}}^s = k_1(2b/\delta^*)(b\underline{n}-\underline{\alpha}^s) \| \dot{\underline{\varepsilon}}^p \| ,$$

$$\dot{\underline{\alpha}}^* = H^*\dot{\underline{\varepsilon}}^p \quad \text{and} \quad \delta = \| b\underline{n}-\underline{\alpha}^s \|$$

By consistency conditions:

$$h = k1(2b/\delta^*)(b\underline{n}-\underline{\alpha}^s) : \underline{n} + H^* + \sqrt{(2/3)}\mu(\bar{R}-R)$$

The isotropic hardening is defined by:

$$\dot{b} = \mu(\bar{b}-b) \| \dot{\underline{\varepsilon}}^p \|$$

$$\dot{R} = \mu(\bar{R}-R) \| \dot{\underline{\epsilon}}^p \|$$

In the present calculations, the cyclically stable values of R and b are used as initial conditions to obtain the cyclically stable response quickly at the outset. This eliminates isotropic hardening which is needed only for modeling transient behavior and makes the hardening purely kinematic.

Values of the constants obtained by fitting the non-linear model to the stress amplitude versus strain range curve for bearing steel estimated by Hahn, Bhargava and Chen (1989) are listed in Table 3 and constants for the ELKP model are listed in Table 2. A description of the NLKP parameters, how they were calculated, and their effects on the shape of the stress amplitude versus strain range curve are described below:

DESCRIPTION OF THE NLKP PARAMETERS

The values of the parameters were calculated from the estimated stress amplitude versus plastic strain range curve in Figure B2. The yield surface is simply the uniaxial yield strength of the material. The cyclically stable amplitude of the short range back stress $\bar{b}$ is calculated by extrapolating the asymptotic plastic response back to the $\Delta\epsilon^p/2$ ordinate. The ordinate for the experimental data is $\Delta\epsilon^p$, so to find $\bar{b}$ the asymptotic plastic response is extrapolated back to $\Delta\epsilon^p$, and the resulting value is divided by 2.

The parameters were modified to obtain the best fit to the experimental curve by subjecting a single plane strain element to cyclic tension and compression and reducing the stress value by 15% to convert the plane strain values to uniaxial stress. The curve was plotted and made to fit the experimental curve.

The parameters in the NLKP model affect the shape of the curve as follows:

$\bar{R}$ - The cyclically stable yield surface radius affects the stress amplitude in the region of small strains.

$\bar{b}$ - The cyclically stable amplitude of the short range backstress affects the stress amplitude in the knee of the curve.

H^* - The coefficient of linear hardening for long range backstress affects the slope of the asymptotic curve.

k1 - The coefficient of short range backstress rate affects how soon the curve reaches its asymptotic value.

μ - The rate constant for isotropic hardening/softening has no effect on the shape of the curve in this model because $b(0) = \bar{b}$ and $R(0) = \bar{R}$ assuming cyclically stable conditions.

Figure B1 Schematic of the Mroz image point, two surface model on non-linear hardening (NLKP).

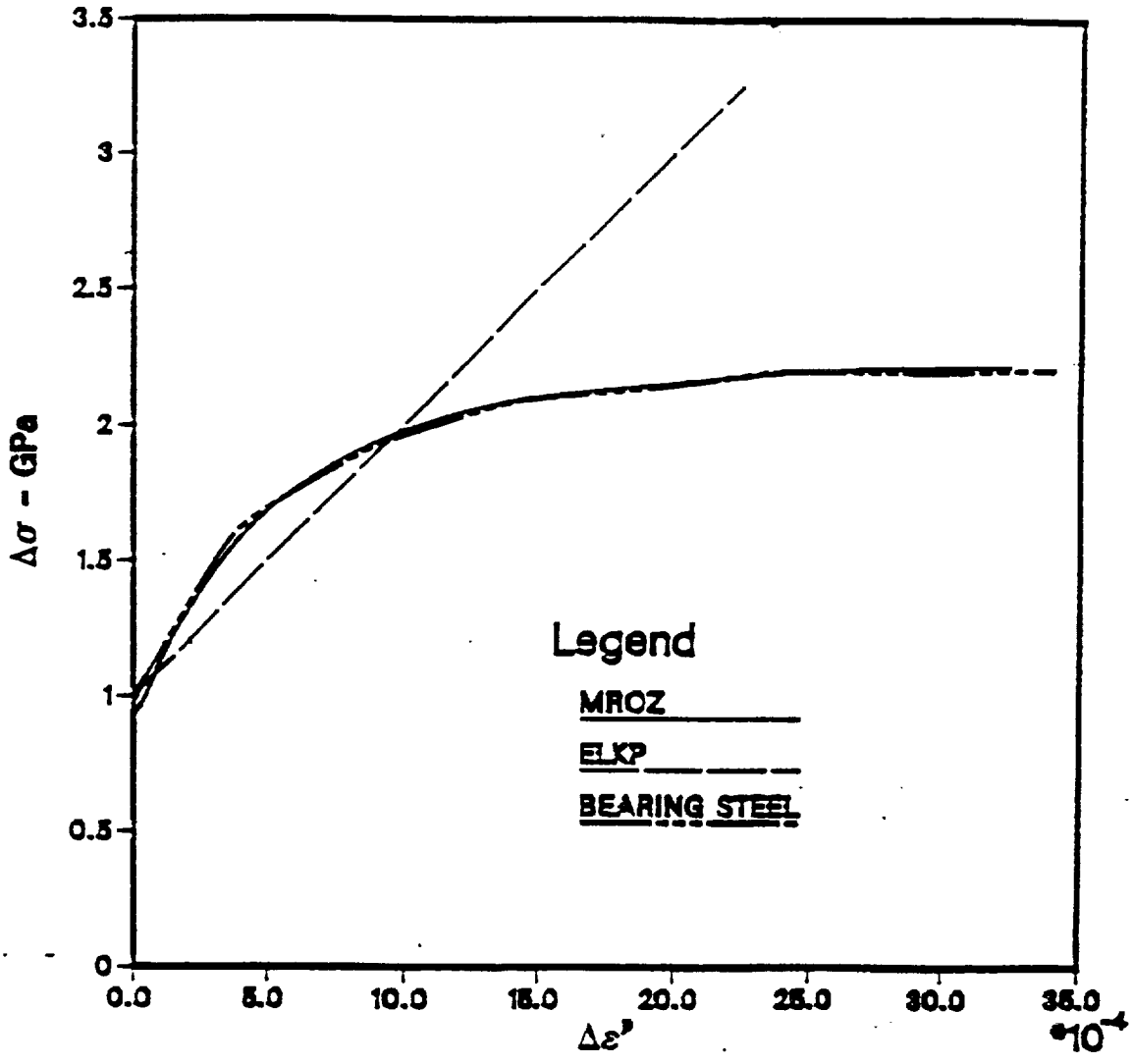

Figure B2 Comparison of the relation between stress amplitude and strain range for: estimated hardened bearing steel corrected for strain rate, NLKP and ELKP.